A methodology for predicting far-field blast loading on structures

Socrates C. Angelides [a,b,*], Colin Morison [c], Bassam A. Burgan [a], Constantinos Kyprianou [a], Samuel E. Rigby [b], Andrew Tyas [b]

[a] *Steel Construction Institute, UK*
[b] *University of Sheffield, UK*
[c] *ColMor Consulting Ltd, UK*

ARTICLE INFO

ABSTRACT

Structural engineers are often tasked with the challenge of enhancing the resilience of buildings and structures to withstand blast loading from the detonation of energetic materials. Such loading typically occurs during terrorist attacks and from accidental explosions in nearby chemical and explosive storage facilities. However, existing methods for predicting the governing blast loading on a structure, through consideration of multiple explosion scenarios, are unsuitable for most practising structural engineers. This paper will address the need for fast-running tools for predicting blast loads on structures in the far-field by presenting the semi-empirical EMBlast method that calculates free-field and reflected pressure-time histories for both the positive and negative phase. For finite size target surfaces, this method also accounts for clearing effects, a phenomenon that results in gradually reducing the reflected pressures on the front face of a building, to the lower free-field pressures experienced by the sides and roof. To validate the predictions of the EMBlast method in the far-field, computational fluid dynamic analyses are performed over a long-range of scaled distances. Furthermore, the EMBlast predictions are also compared with the results from published blast tests, existing empirical methods and computational fluid dynamic simulations identified in the literature.

1. Introduction

The 2020 explosion initiating at the Port of Beirut, where large quantities of stored explosive material accidentally detonated, resulted in severe damage to many buildings and structures situated a few kilometres away [1]. As a result of urbanisation, numerous buildings and structures are now located near petrochemical, chemical and explosive storage facilities, and therefore are at risk from accidental explosions. Additionally, the increasing number of terrorist attack incidents observed globally further highlight the vulnerability of our built environment to explosions. Consequently, structural engineers are now often tasked with the challenge of enhancing the resilience of buildings and structures to withstand blast loading. This typically involves replacing the weak monolithic glass elements in the building envelope with the more ductile laminated glass panels [2] and designing key structural elements to resist the intense dynamic pressures resulting from an explosion [3]. However, due to the uncertain nature of the threat, the governing blast loading on a structure can only be determined by considering multiple explosion scenarios. Where the explosion results

from the detonation of energetic materials (i.e. high-explosives), this is done by varying the explosive charge mass (W) and standoff distance (R) between the charge and the structure to determine the resulting blast loading on the structure for each case. Where the explosion results from ignition of a vapour cloud (e.g. following an accidental release of a hydrocarbon gas in a petrochemical plant), the situation is more complex, as it involves many variables, such as the gas release location, its dispersion into the atmosphere, the ignition point / time and the interaction of the flame front with obstacles it encounters. The remainder of this paper will focus only on energetic materials detonations.

The free-field (also referred to as incident or side-on) blast wave pressure-time history at a fixed distance from the detonation of an energetic material is characterised by high overpressures developed instantaneously, followed by a decay that may result in negative overpressure (below ambient pressure). The negative phase of the blast wave has a longer duration compared to the positive phase, but a lower pressure in absolute value [4]. The blast wave is followed by a blast wind, analogous to natural wind, therefore causing dynamic (also known as drag) pressures to act on the objects that it encounters in its
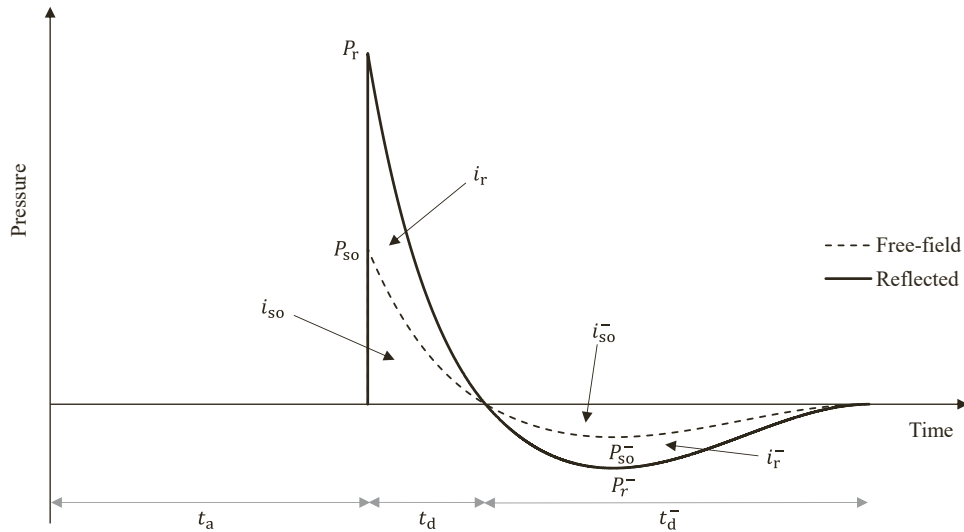
Fig. 1. Pressure-time history at a target point, indicating the free-field and reflected blast parameters.
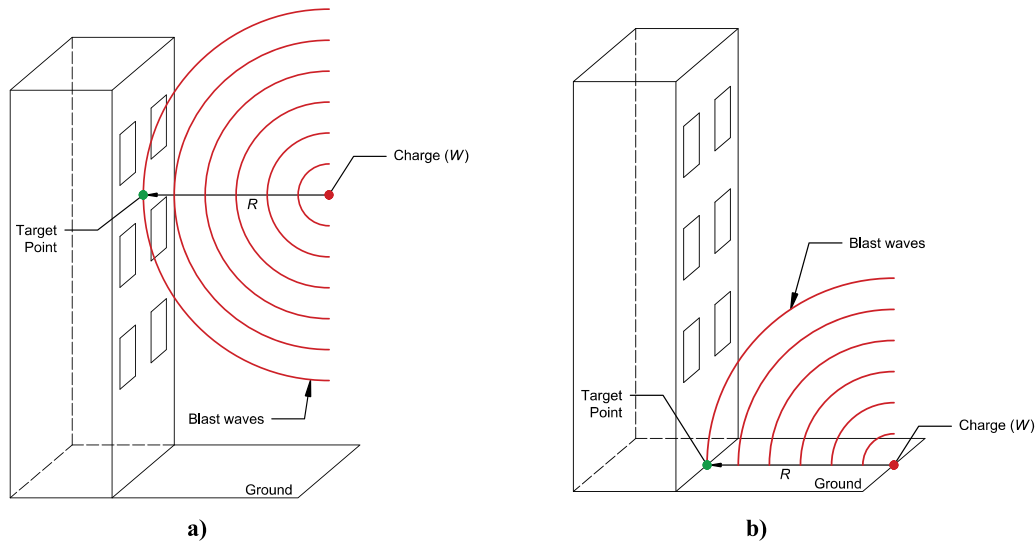

Fig. 2. a) Free-air burst (spherical charge), b) soft ground surface burst (hemi-spherical charge).

path. These pressures are significantly higher and of shorter duration compared to those produced by natural winds. Dynamic pressure is additive to the overpressure from the blast wave and is not dominant for large surfaces. On the other hand, for small structures that are immediately engulfed by the blast wave and result in the cancelation of overpressure, blast wind governs the blast loading. When the free-field blast wave impinges on an infinite surface structure, the wave is reflected, resulting in an amplified pressure-time history, as shown in Fig. 1. The key blast parameters are labelled in Fig. 1, indicating the blast wave time of arrival t_a, positive t_d and negative t_d^- phase durations, peak positive free-field P_{so} and reflected P_r pressures, peak negative free-field P_{so}^- and reflected P_r^- pressures, positive free-field i_{so} and reflected i_r impulses, and free-field i_{so}^- and reflected i_r^- negative impulses. The free-field parameters are denoted with the subscript 'so' and the reflected with the subscript 'r'. Clearing effects influence the pressure-time history experienced by surface structures of finite size. This is a phenomenon that results in gradually reducing the reflected pressures on the front face of a building, to the lower stagnation pressure, which is the combined free-field and dynamic pressure experienced by the sides and roof [5].

The positive phase parameters can be derived empirically from the Kingery & Bulmash polynomial equations that have been fitted to free-air (spherical charges – refer to Fig. 2a) and soft ground surface burst (hemi-spherical charges – refer to Fig. 2b) blast trials with Trinitrotoluene (TNT) charges, as a function of the scaled distance $Z = R/W^{1/3}$ [6]. These equations have been implemented in military standards and are included in the appendix of UFC 3–340–01 [7] and presented in the form of graphs in UFC 3–340–02 [8]. Furthermore, these empirical equations form the basis of CONWEP [9], a US blast loading predictive software. UFC 3–340–02 also includes graphs with reflection coefficients C_r for deriving the peak reflected pressures $P_{r,\theta} = C_r P_{so}$ when the front of the blast wave is at an oblique angle to a reflecting surface. Reflection coefficients are available for angles of incidence θ ranging from 0° to 90° and these are derived as a function of the peak free-field pressure P_{so}. Similarly, reflected impulse $i_{r,\theta}$ values are also available for the same range of angles of incidence. UFC 3–340–02 includes an empirical equation for calculating the "clearing time", i.e. the duration over which the reflected pressure linearly decays to the stagnation pressure. However, a comparison with numerical results has demonstrated that the UFC clearing method is only valid for targets of scaled height Z/250 and smaller [10]. UFC 3–340–02, and its previous revision TM5–1300 [11], also include graphs for deriving the negative phase parameters.
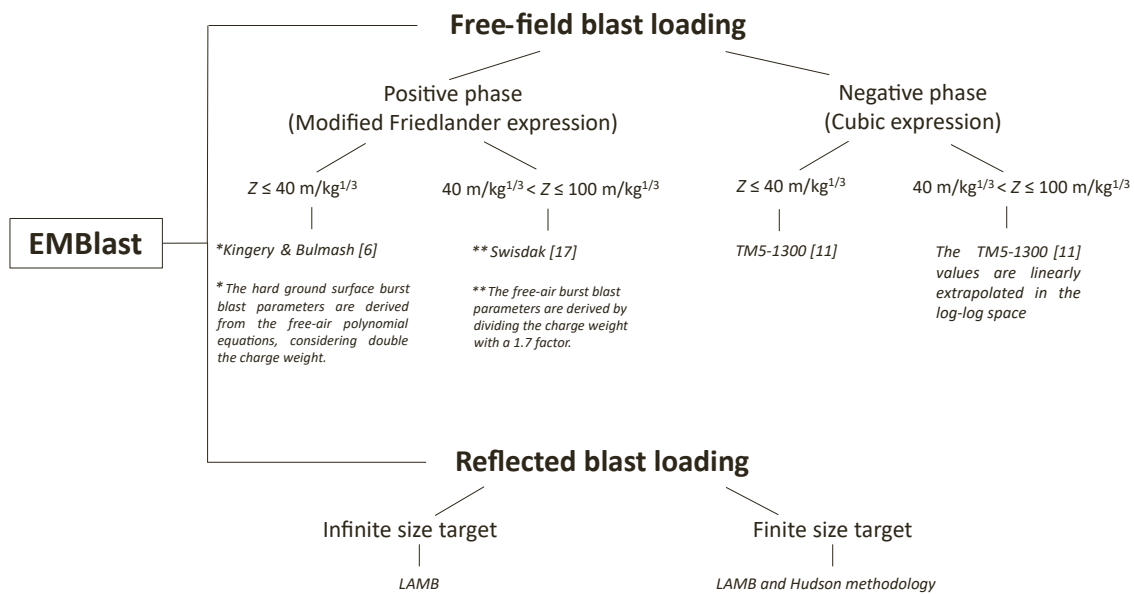
Fig. 3. Diagram summarising the EMBlast methodology.

However, the original source of these graphs is unclear, with Rigby et al. [4] suggesting that these may have been initially derived analytically, and later supplemented with experimental data. Graphs are not available in UFC 3–340–02 for the negative phase parameters as a function of the angle of incidence; instead, it is recommended to derive these at fictitious scaled distances Z_P* and Z_i* corresponding to positive normally reflected values that are equal to the oblique positive parameters, i.e. $P_r(Z_P*) = P_{r,\theta}$ and $i_r(Z_i*) = i_{r,\theta}$. Nevertheless, recent full-scale blast testing investigations suggested that the far-field negative phase parameters are independent of angle of incidence [12]. The phase parameters for other explosive types can also be derived empirically by converting in the scaled distance formula the explosive weight to a TNT equivalent weight. Empirical TNT equivalence factors can be specified by the explosive manufacturer or obtained from standards such as ISO/FDIS 16933 [13] and ASCE / SEI 59–22 [14]. Alternatively, these can be derived from first-principles by considering the Berthelot Method, the Cooper Method, the Hydrodynamic Work, the Explosive Power (i.e. Power Index) or the Heat of Detonation. The latter is the most commonly used method for industry purposes and is recommended by UFC 3–340–02 [15,16]. Once the phase parameters have been derived, the pulse shape can be linearly approximated for design purposes, with a right triangular pressure-time history, i.e. a linearly decaying straight line, assumed for the positive phase [8]. Alternatively, more refined pulse shapes can be assumed for the positive and negative phase of the blast loading, such as the modified Friedlander equation and cubic expression, respectively [4] shown in Fig. 1. Such empirical methods for deriving blast loads on buildings and structures are significantly faster compared to the numerical methods described below. However, the Kingery & Bulmash [6] positive phase polynomial equations and the TM5–1300 negative phase graphs are limited to scaled distances up to $Z = 40$ m/kg$^{1/3}$ in the far-field. The UFC 3–340–02 negative phase parameter graphs are limited to even smaller scaled distances. Swisdak [17] extended the polynomial equations for calculating positive phase peak free-field pressure P_{so} and impulse i_{so} values up to scaled distances of $Z = 198.5$ and 158.7 m/kg$^{1/3}$, respectively, by fitting polynomials to far-field surface burst (hemispherical charges) blast trials [18]. However, polynomial equations for calculating far-field reflected blast parameters are not available.

The blast loading on structures can also be derived numerically with Computational Fluid Dynamics (CFD) analyses. Free-field and reflected pressure-time histories can be predicted in the far-field beyond the empirical limits. Furthermore, complex urban environments can be modelled to account for the reflection of blast waves on multiple buildings [19]; this is not accounted for in the simplified empirical methods. However, CFD analyses require considerable user experience and significantly longer computation times compared to the empirical methods rendering them sometimes unsuitable for practitioners. To reduce the computation time, Shin et al. [20] fitted polynomial equations for positive phase blast parameters to CFD analyses performed with Autodyn. Free-air (spherical charges) CFD analyses were simulated up to a scaled distance of $Z = 40$ m/kg$^{1/3}$ in the far-field. Comparing the CFD predictions with the Kingery & Bulmash [6] empirical results, Shin et al. concluded that the empirical equations overpredict the CFD calculations of incident impulse i_{so} and positive duration t_d in the far-field by 10–25% and 10–20%, respectively. This was also observed by Taylor [21], who performed surface burst CFD analyses with ALE3D up to a scaled distance of $Z = 100$ m/kg$^{1/3}$ in the far-field, assuming hard ground conditions and adopting a factor of 2 on the charge mass (W) to account for the effect of perfect ground amplification. Taylor's CFD incident impulse i_{so} predictions consistently underpredicted the results from Swisdak's [17] extended empirical polynomial equations in the far-field.

This paper will address the need for fast-running tools for predicting blast loads on structures in the far-field by presenting the semi-empirical method implemented in the EMBlast blast loading software, hereafter referred to as the EMBlast method and described in Section 2. In the EMBlast method, free-field blast parameters are derived from existing empirical polynomial equations that are further extended in the far-field for both the positive and negative phase. To derive the reflected blast waves on structures, the free-field waves are superimposed non-linearly, following the Low Altitude Multiple Burst (LAMB) shock addition rules, with target-reflected waves assumed to originate from fictitious charges (image). This is a semi-empirical method initially developed in the 1970 s for combining blast waves originating from nuclear detonations [22]. The LAMB shock addition rules are also referred to in the appendix of UFC 3–340–01 as a recommended method for deriving the combined pressure-time history from energetic material detonations produced by multiple explosions or from the numerous reflections on walls in a confined room scenario. In contrast to the existing empirical methods described above, the LAMB method has the advantage of predicting far-field positive and negative phase reflected pressure-time histories. Clearing effects on finite size targets are accounted for in the EMBlast method with the Hudson methodology, by superimposing the reflected pressure-time histories with pressure relief waveforms travelling from the edges. This is a first-principles approach for predicting clearing
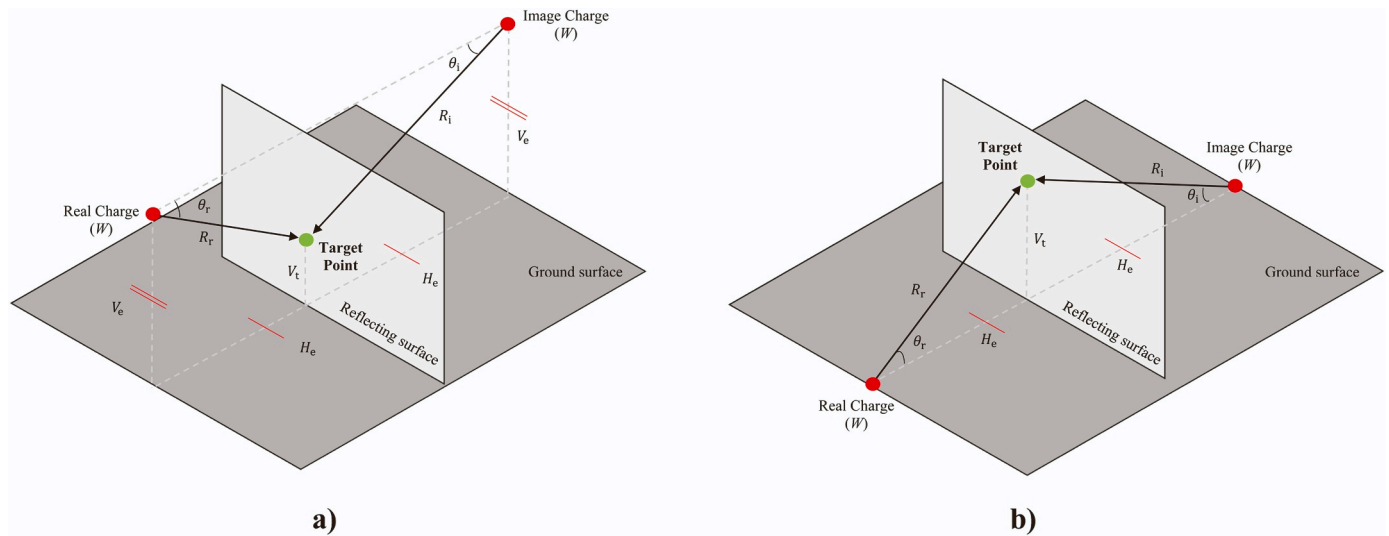
Fig. 4. Sketches of image bursts for LAMB addition: a) free-air burst (spherical charge), b) surface burst (hemi-spherical charge).

effects, originally developed by Hudson [23] that was later extended and validated by many researchers [10,24–26]. In contrast to the UFC clearing method described above, the Hudson methodology is not limited to small scaled height targets.

To validate the predictions of the EMBlast method in the far-field, CFD analyses are performed over a long-range of scaled distances as described in Section 3. The key blast parameters described above were recorded in each CFD analysis, to allow a direct comparison with the EMBlast predictions. Furthermore, the EMBlast predictions are also compared with the results from published open-arena full-scale blast tests. For infinite target surfaces, the key blast parameter predicted by EMBlast are compared with the experimental results presented by Rigby, et al. [12], who performed blast tests with PE4 charges placed on a concrete slab, with the charge mass ranging from $180\ \text{g} \leq W \leq 350\ \text{g}$, the standoff distance from $2\ \text{m} \leq R \leq 6\ \text{m}$ and the angle of incidence from $0° \leq \theta \leq 56°$. The key blast parameters are presented in this published experimental work, which have been calculated by the authors by post-processing the recorded pressure-time history. The EMBlast pressure-time history predictions on finite surfaces, which include clearing effects, are compared with the recorded pressure-time histories presented by Tyas, et al. [24], who performed blast tests with $W = 250\ \text{g}$ PE4 charges placed on a concrete slab. The pressure-time histories were recorded by two gauges placed on a reinforced concrete block target of height 675 mm and width 710 mm, with the standoff distance ranging from $4\ \text{m} \leq R \leq 10\ \text{m}$. These comparisons, along with the results from the existing empirical methods and CFD simulations identified in the literature and discussed above, are presented in Section 4.

2. EMBlast model description

The methodology for deriving the free-field and reflected blast parameters and pressure-time histories is introduced in this section. Three burst types are considered, namely free-air, soft-ground surface and hard-ground surface explosions. Fig. 3 presents a summary of the EMBlast methodology.

2.1. Free-field blast loading

The free-field free-air and soft ground surface burst blast parameters for the positive phase up to scaled distances $Z \leq 40\ \text{m/kg}^{1/3}$ are derived from the Kingery & Bulmash [6] empirical equations. For far-field scaled distances $40\ \text{m/kg}^{1/3} < Z \leq 100\ \text{m/kg}^{1/3}$, Swisdak's [17] empirical equations are implemented in EMBlast for deriving the peak free-field pressure P_{so} and impulse i_{so}. To convert Swisdak's surface charge

polynomials to equivalent free-air explosions, the charge weight is divided by a 1.7 factor that removes the ground amplification effect. This assumes soft ground conditions, with part of the energy absorbed by the ground. Linear equations are implemented in EMBlast at a scaled distance of $Z = 40\ \text{m/kg}^{1/3}$ to create a smooth transition between the polynomials derived from two different sources (i.e. Kingery & Bulmash and Swisdak). The time of arrival t_{a} of the blast waves in the far-field is calculated from a linear extrapolation of the time of arrival t_{a} at a scaled distance of $Z = 40\ \text{m/kg}^{1/3}$, assuming a constant blast wave front velocity of 343 m/s. The Kingery & Bulmash free-air burst polynomial equations for wave front velocities converge to this value for scaled distances greater than $Z \geq 31\ \text{m/kg}^{1/3}$. The hard ground surface burst blast parameters are derived from the free-air polynomial equations, considering a modified scaled distance with double the charge weight ($2W$) to account for perfect ground amplification. Finally, the positive phase free-field pressure-time history $p_{\text{so}}^{+}(t)$ at a target point is described by the modified Friedlander expression, given by Eq. (1a):

$$p_{\text{so}}^{+}(t) = P_{\text{so}}\left[1 - \frac{t}{t_{\text{d}}}\right]e^{-\frac{bt}{t_{\text{d}}}} \quad t \leq t_{\text{d}} \tag{1a}$$

where, P_{so} is the peak free-field pressure, t is the time, t_{d} is the positive time duration and b is the decay factor. The decay factor b is calculated iteratively by setting the integral of the modified Friedlander equation with respect to time to be equal to the impulse value i_{so}. This decay factor approaches zero at the scaled distance of $Z = 40\ \text{m/kg}^{1/3}$. Therefore, a linear relationship is assumed for the positive phase pressure-time history at the far-field scaled distances $Z > 40\ \text{m/kg}^{1/3}$ and the positive phase duration t_{d} is then calculated by setting the integral of this linear equation to be equal to the impulse value i_{so}.

The negative phase parameters up to scaled distances $Z \leq 40\ \text{m/kg}^{1/3}$ are derived from TM5–1300, by digitising Figures 2.8 and 2.16 and fitting polynomial equations to these digitised points. The negative peak pressure p_{so}^{-} and impulse i_{so}^{-} graphs are then linearly extrapolated in the log-log space to scaled distances up to $Z = 100\ \text{m/kg}^{1/3}$. The fitted and extrapolated polynomial equations, for both free-air and soft-ground surface bursts, are presented in Appendix A.1. A modified scaled distance with double the charge weight ($2W$) is considered for the derivation of the hard ground surface burst blast negative phase parameters. The negative phase pressure-time history $p_{\text{so}}^{-}(t)$ at a target point is described by the cubic expression given by Eq. (1b):

$$p_{\text{so}}^{-}(t) = -P_{\text{so}}^{-}\left(\frac{6.75(t - t_{\text{d}})}{t_{\text{d}}^{-}}\right)\left(1 - \frac{(t - t_{\text{d}})}{t_{\text{d}}^{-}}\right)^{2} \quad t_{\text{d}} < t \leq t_{\text{d}} + t_{\text{d}}^{-} \tag{1b}$$
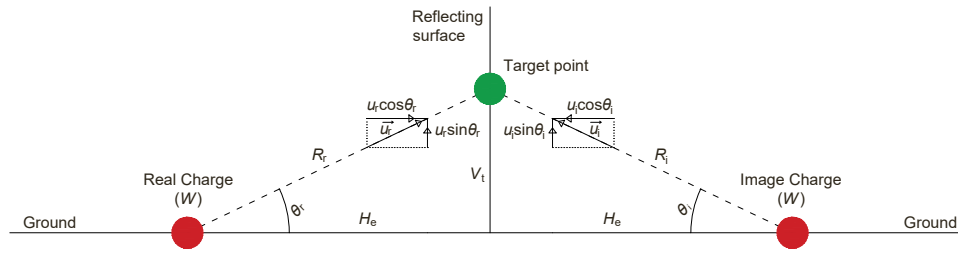
Fig. 5. Decomposition of the velocity vectors of the real and image waves into horizontal and vertical components for a surface burst.
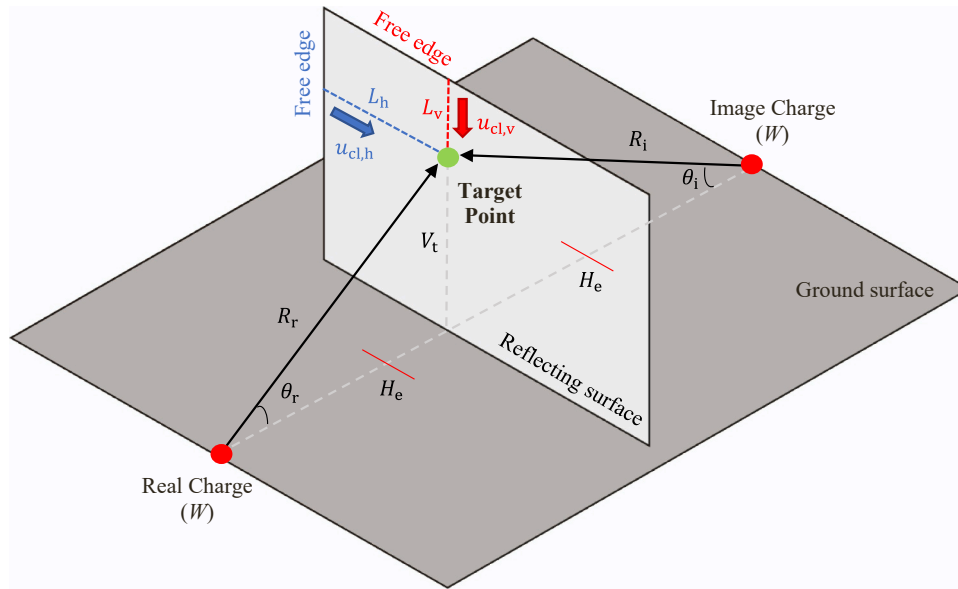

Fig. 6. Sketch indicating the propagation of pressure-relief clearing waves from the free edges towards the target point.

where, p_{so}^{-} is the negative peak pressure, t is the time, t_d is the positive time duration and t_d^{-} is the negative time duration. The latter is calculated iteratively by setting the integral of the cubic expression equation, with respect to time, to be equal to the impulse value i_{so}^{-}.

Therefore, the combined free-field pressure-time history $p_{so}(t)$ is given by Eq. (1c):

$$p_{so}(t) = \begin{cases} p_{so}^{+}(t) & t \le t_d \\ p_{so}^{-}(t) & t_d < t \le t_d + t_d^{-} \end{cases} \tag{1c}$$

2.2. Reflected blast loading

This section presents the methodology for calculating reflected pressure-time histories on infinite and finite target surfaces. The resulting blast loading differs due to the clearing effects that are ignored in the former.

2.2.1. Infinite targets

LAMB is an algorithm for combining blast waves that was created to provide fast approximate loading resulting from multiple nuclear burst scenarios, without requiring time integrations [22]. In the EMBlast method, the LAMB shock addition rules are adopted for deriving the reflected pressure-time history at a target point on an infinite, rectangular planar surface following the detonation of an energetic material. This is achieved by combining the incident wave to the target point with a target-reflected wave resulting from the reflection of the incident wave on the target surface. The former is the free-field blast wave described in Section 2.1, and the latter is assumed to originate from a fictitious charge (image) of identical weight to the actual charge (real) and

located symmetrically to the actual charge (real), with respect to the target surface, as shown in Fig. 4. A similar image burst approach is described in the LAMB manual [22] for representing the reflection of free-field waves on the ground. In both cases, the structure and the ground are assumed infinitely rigid, ignoring any energy absorbed. The real $p_{so,r}(t)$ and image $p_{so,i}(t)$ waves are combined using the LAMB shock addition rules and the reflected pressure-time history is derived from Eq. (2):

$$p_r(t) = p_{so,r}(t) + p_{so,i}(t) + 1.2[q_r(t) + q_i(t) - \overline{q}(t)] \tag{2}$$

where, $\overline{q}(t)$ is a modification factor, $p_{so,r}(t)$ and $p_{so,i}(t)$ are the incident pressure-time histories, $q_r(t)$ and $q_i(t)$ are the dynamic pressure-time histories, for the real and image waves, respectively.

This is a semi-empirical equation providing good agreement with CFD simulations and experimental measurements for a wide range of multiple burst scenarios that is not fully-supported from first-principles, but is based on the conservation of mass, momentum, and energy. The modification factor $\overline{q}(t)$ ensures that the resultant kinetic energy is less than the sum of the individual kinetic energies from the real and image waves and is provided in Eq. (3a):

$$\overline{q}(t) = \frac{1}{2}\overline{\rho}(t)\overline{u}(t)^2 \tag{3a}$$

The density $\overline{\rho}(t)$ and the velocity $\overline{u}(t)$ are given by Eq. (3b) and (3c.1), respectively:
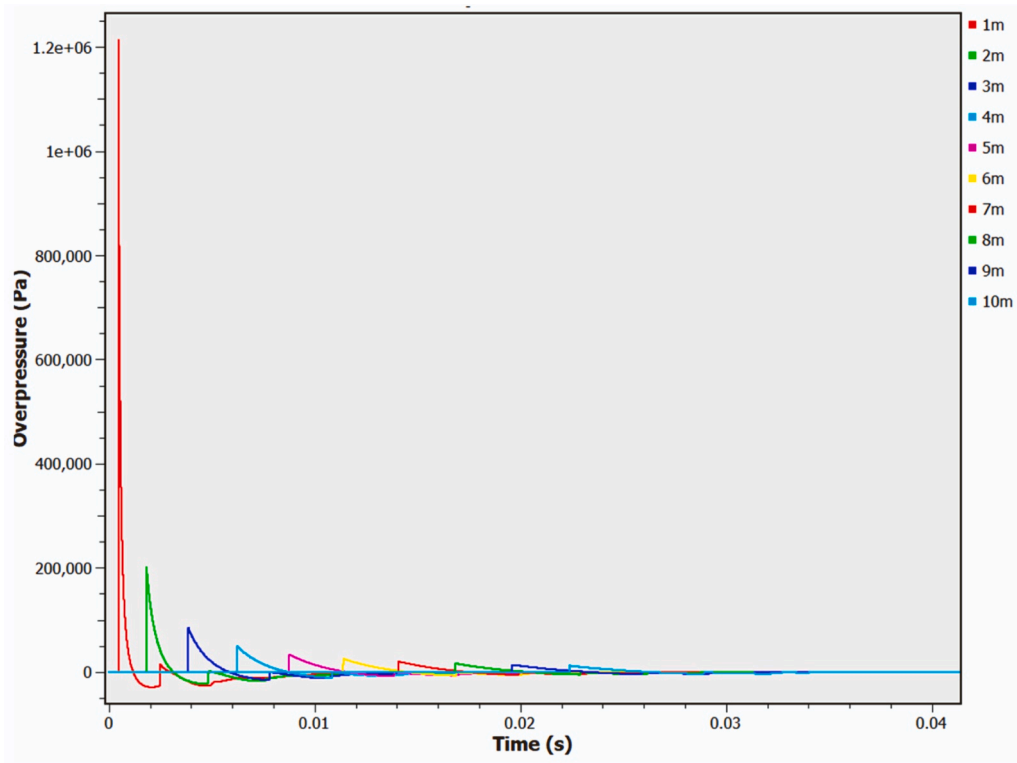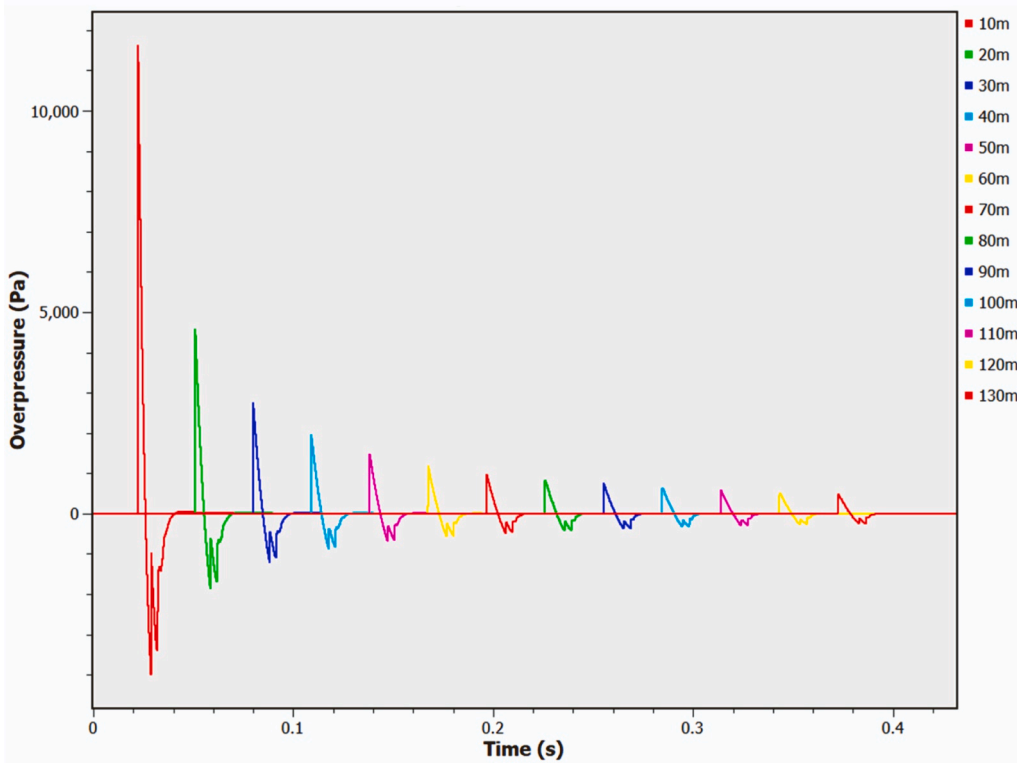
$$\overline{\rho}(t) = \rho_0 + \rho_r(t) - \rho_0 + \rho_i(t) - \rho_0 \tag{3b}$$

Fig. 7. Viper CFD free-field pressure time histories: a) scaled distances 1 m/kg$^{1/3}$ $\leq$ Z $\leq$ 10 m/kg$^{1/3}$, b) scaled distances 10 m/kg$^{1/3}$ $\leq$ Z $\leq$ 130 m/kg$^{1/3}$.

Table 1

Comparison of the 1D Viper CFD free-field positive blast parameters with the Kingery & Bulmash [6] empirical values.

SCALED DISTANCE, Z [m/kg$^{1/3}$]	PEAK PRESSURE, P_{so} [kPa]			PEAK IMPULSE, i_{so} [kPa-msec]		
	Viper CFD	Kingery & Bulmash [6]	[%]	Viper CFD	Kingery & Bulmash [6]	[%]
1	1214.041	934.861	130	141.584	174.543	81
2	201.506	194.700	104	81.031	91.120	89
3	83.756	81.590	103	59.603	64.330	93
4	48.850	46.540	105	46.291	49.790	93
5	33.346	31.296	107	37.586	40.619	93
6	24.862	23.200	107	31.553	34.290	92
7	19.602	18.320	107	27.154	29.660	92
8	16.062	15.080	107	23.817	26.140	91
9	13.534	12.790	106	21.202	23.370	91
10	11.648	11.091	105	19.100	21.131	90
20	4.593	4.451	103	9.568	10.752	87
30	2.752	2.533	109	6.376	7.162	89

$$\overline{u}(t) = \frac{\overrightarrow{u}_r(t)\rho_r(t)}{\overline{\rho}(t)} + \frac{\overrightarrow{u}_i(t)\rho_i(t)}{\overline{\rho}(t)} \tag{3c.1}$$

where, ρ_0 is the ambient air density (1.225 kg/m^3), $\rho_r(t) - \rho_0$ and $\rho_i(t) - \rho_0$ are the overdensities (i.e. densities above the ambient air densities), $\rho_r(t)$ and $\rho_i(t)$ are the densities, and $\overrightarrow{u}_r(t)$ and $\overrightarrow{u}_i(t)$ are the vector velocities, of the real and image waves, respectively.

As shown in Fig. 5, the vector velocities of the real and image waves can be resolved according to Equation (3c.2):

$$\overline{u}(t) = \frac{(\sin\theta_r + \cos\theta_r)u_r(t)\rho_r(t)}{\overline{\rho}(t)} + \frac{(\sin\theta_i - \cos\theta_i)u_i(t)\rho_i(t)}{\overline{\rho}(t)} \tag{3c.2}$$

where, $u_r(t)$ and $u_i(t)$ are the velocity magnitudes, and θ_r and θ_i are the angles of incidence, of the real and image waves, respectively.

As shown in Fig. 4, both charges have the same vertical distance to the ground (V_e) and horizontal distance to the reflecting surface (H_e). Therefore, the standoff distance between both charges and any target point is the same, i.e. $R_r = R_i$, resulting in two identical waves, i.e. $p_{so,r}(t) = p_{so,i}(t)$, $q_r(t) = q_i(t)$, $\rho_r(t) = \rho_i(t)$, $u_r(t) = u_i(t)$ and $\theta_r = \theta_i$, arriving at the same time from opposite directions at the target point. The reflected pressure-time history and the modification factor can then be simplified, as show in Eqs. (4a) and (4b), respectively:

$$p_r(t) = 2p_{so,r}(t) + 1.2(2q_r(t) - \overline{q}(t)) \tag{4a}$$

$$\overline{q}(t) = \frac{1}{2}[2\rho_r(t) - \rho_0]\left[\frac{2\sin\theta_r u_r(t)\rho_r(t)}{2\rho_r(t) - \rho_0}\right]^2 \tag{4b}$$

For ideal gas conditions and a normally reflected blast wave, i.e. $\theta_r = 0$, Eq. (4a) reduces to the Rankine-Hugoniot solution for the peak reflected pressure P_r. Applying the Rankine-Hugoniot conditions at the blast wave front, the peak dynamic pressure $q_{r,peak}$, density $\rho_{r,peak}$ and velocity $u_{r,peak}$ of the real wave can be related to the peak free-field overpressure $P_{so,r}$, as shown in Eqs. (5a), (5b) and (5c), respectively:

$$q_{r,peak} = \frac{1}{2}\rho_{r,peak}u_{r,peak}^2 \tag{5a}$$

$$\rho_{r,peak} = \rho_0 \frac{\left(\frac{\gamma_s+1}{\gamma_s-1}\right)\frac{P_{so,r}}{P_0} + \frac{2\gamma_s}{\gamma_s-1}}{\frac{P_{so,r}}{P_0} + \frac{2\gamma_0}{\gamma_0-1}} \tag{5b}$$

$$u_{r,peak} = c_0\left[\frac{2P_{so,r}}{\gamma_0 P_o}\left(\frac{P_{so,r} + P_0\frac{\gamma_0-\gamma_s}{\gamma_0-1}}{(\gamma_s+1)P_{so,r} + 2\gamma_s P_0}\right)\right]^{0.5} \tag{5c}$$

where, c_0 is the speed of sound in air (343 m/s), γ_0 is the ambient air

specific heat ratio, P_0 is the ambient atmospheric pressure (101.325 kPa at sea level), γ_s is the shocked air specific heat ratio (typically taken as 1.4 in the far-field, but ranges from 1.17 to 1.67. Refer to UFC 3–340–01 for an approximation at sea level in the near-field as a function of the peak free-field overpressure $P_{so,r}$).

The Rankine-Hugoniot conditions do not hold behind the blast wave front. In the EMBlast method, the pressure q_r, density ρ_r and velocity u_r time histories behind the blast wave front are derived from the UFC 3–340–01 approximations shown in Eqs. (6a), (6b) and (6c), respectively that are described as reasonably accurate for far-field explosions unaffected by the detonation products:

$$q_r(t) = q_{r,peak}\left[\frac{\frac{\rho_{r,peak}}{\rho_0}\left(\frac{p_{so,r}(t)+P_0}{P_{so,r}+P_0}\right)^{1/\gamma_0} - 1}{\frac{\rho_{r,peak}}{\rho_0} - 1}\right]\frac{p_{so,r}(t)}{P_{so,r}} \tag{6a}$$

$$\rho_r(t) = \rho_{r,peak}\left[\frac{p_{so,r}(t) + P_0}{P_{so,r} + P_0}\right]^{1/\gamma_s} \tag{6b}$$

$$u_r(t) = \left[\frac{2q_r(t)}{\rho_r(t)}\right]^{0.5} \tag{6c}$$

Following comparisons with CFD analyses and experimental data, the following modifications to the LAMB rules are implemented into the EMBlast method:

- In rare cases the sum of the overdensities may be negative and greater in magnitude than the ambient density. To avoid a non-physical negative density $\overline{\rho}(t)$ in such cases, a simple superposition rule is applied for deriving the reflected pressure-time history as the direct sum of the overpressures from the two contributing blast waves, i.e. $p_r(t) = 2p_{so,r}(t)$.
- The total negative pressure (p_r^-) at a target point at any time cannot exceed in absolute value the sum of the negative pressures from the two contributing blast waves, i.e. $2p_{so,r}^-(t)$, the negative ambient atmospheric pressure ($-P_0 = -101.325$ kPa) or the sum of the negative pressures from the contributing blast waves $2p_{so,r}^-(t)$ multiplied by a factor equal to $\max(\frac{2.0287+0.0106\overline{p}_{min}}{2}, 1)$, where p_{min}^- is the largest negative pressure value at that time from the two contributing blast waves. The latter restriction bounds linearly the reflection coefficient of the negative pressure from 2 at low pressures to 1 when the negative ambient atmospheric pressure is reached.
- The total dynamic pressure from each contributing blast wave minus the modification factor $2q_r(t) - \overline{q}(t)$ should not be a negative value. For such cases, a simple superposition rule is applied for deriving the reflected pressure-time history as the direct sum of the overpressures from the two contributing blast waves, i.e. $p_r(t) = 2p_{so,r}(t)$.

Finally, the reflected impulses i_r and i_r^- are calculated by integrating the positive and negative phase of the reflected pressure-time history, respectively.

2.2.2. Finite targets

The reflected pressure-time histories derived using the LAMB methodology correspond to an infinitely large structure. For structures of finite size, these reflected pressures are influenced by clearing effects, a phenomenon that results in gradually reducing the reflected pressures on the front face of a structure to the lower free-field pressures experienced by the sides and roof. In the EMBlast method, the Hudson clearing methodology is adopted. This is a first-principles approach to account for clearing effects by superimposing the reflected pressure-time history calculated at a target point assuming that it is located on an infinite surface, with pressure relief waveforms travelling from the free edges of a finite target surface. Hudson [23] derived pressure relief waveforms
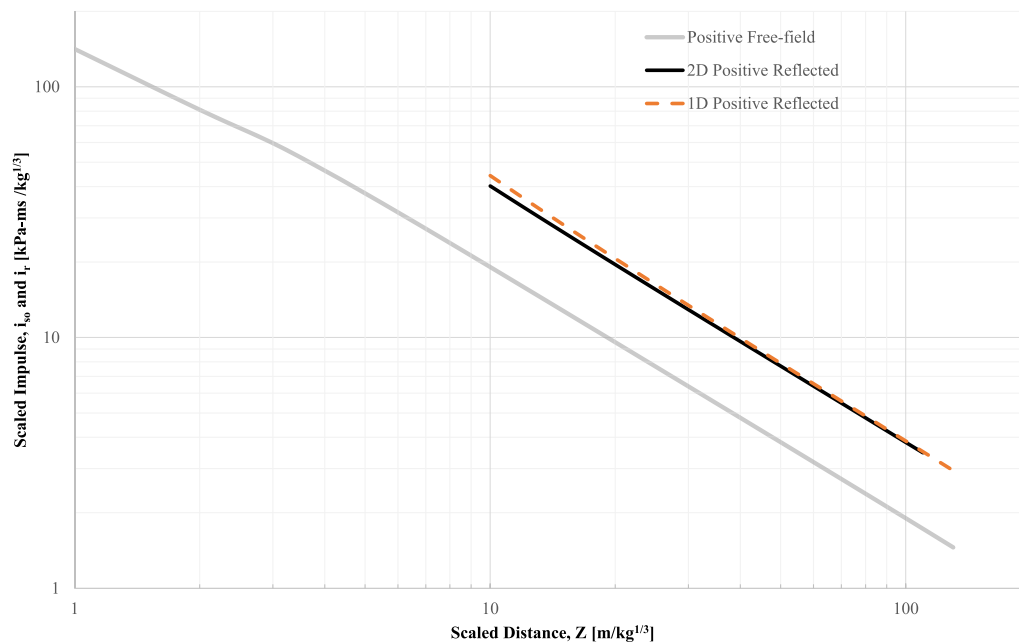
a)
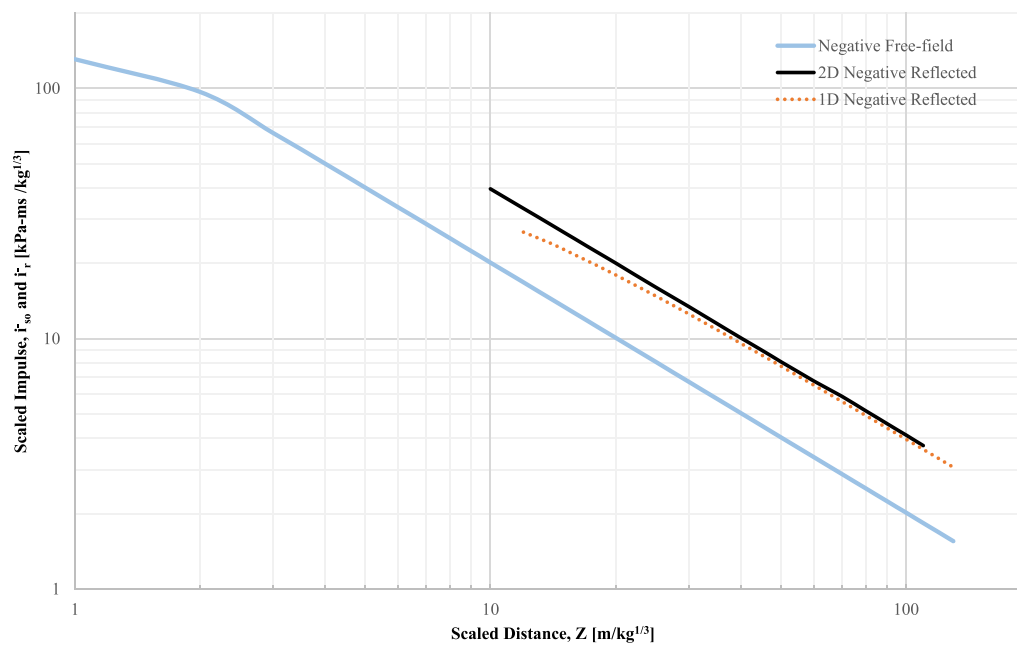
b)

Fig. 8. Comparison of scaled impulse results from 1D and 2D Viper reflection analyses: a) positive phase, b) negative phase.

using the Sommerfeld diffraction theory and presented these in graphical form as a function of a nondimensional length $\eta = L/\lambda$, where L is the distance of the target point to the nearest free edge (shown as L_h and L_v in Fig. 6 indicating the distances to the nearest horizontal and vertical free edges, respectively) and λ is the spatial length of the positive phase of the free-field pressure-time history. The latter is derived as the product of the pressure relief wave speed u_{cl} (shown as $u_{cl,h}$ and $u_{cl,v}$ in Fig. 6 indicating the speed of the pressure relief waves travelling from the nearest horizontal and vertical free edges, respectively) times the positive phase duration t_d. For far-field explosions, the pressure relief wave speed u_{cl} typically converges to the ambient sound speed

(343 m/s). In the EMBlast method, the pressure relief wave speed u_{cl} is calculated from the analytically derived equation by Nartu et al. [26] and presented in Eq. (7) that has shown good agreement with CFD results for scaled distances $Z \geq 2$ m/kg$^{1/3}$:

$$u_{cl}(t) = c_0 \left[\frac{p_r(t) + P_o}{P_o} \right]^{\frac{\gamma_s - 1}{2\gamma_s}} \qquad (7)$$

where, c_0 is the speed of sound in air (343 m/s), P_0 is the ambient atmospheric pressure (101.325 kPa at sea level) $p_r(t)$ is the reflected pressure-time history calculated at a target point on an infinite surface
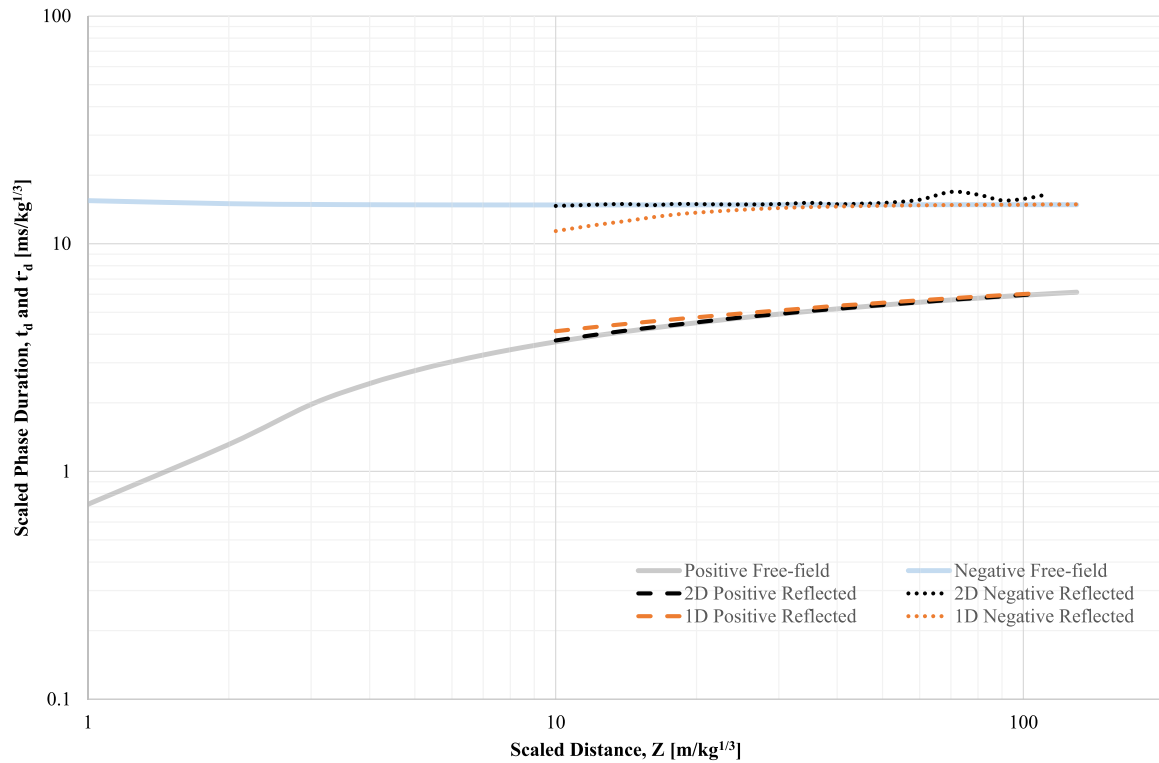
Fig. 9. Comparison of scaled phase duration results from 1D and 2D Viper reflection analyses.
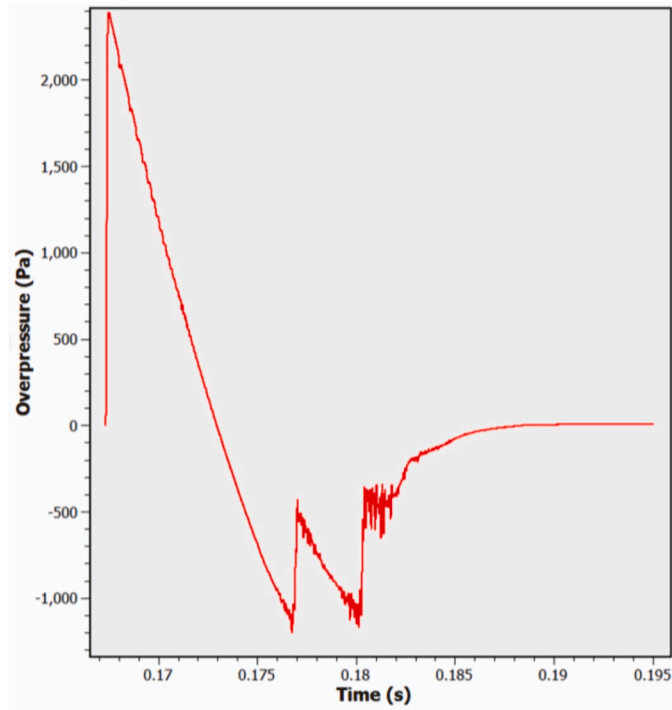

Fig. 10. 2D reflected pressure-time history curve at scaled distance $Z = 60$ m/kg$^{1/3}$.

and derived from LAMB addition (refer to Section 2.2.1), γ_s is the shocked air specific heat ratio (typically taken as 1.4 in the far-field, but ranges from 1.17 to 1.67. Refer to UFC 3–340–01 for an approximation at sea level in the near-field as a function of the peak free-field overpressure $P_{so,r}$).

Table 2
Sensitivity of the reflected negative phase duration relative to free-field value with variation of the CFL number.

STANDOFF DISTANCE, R [m]	COURANT-FRIEDRICHES-LEWY (CFL)					
	0.26	0.24	0.22	0.20	0.18	0.16
50		1.028	1.009	1.019	1.025	1.037
60	1.009	1.018	1.029	1.052	1.095	1.217
70			1.063	1.140	1.111	1.577
80			1.038	1.107	1.059	1.071
90			1.014	1.045	1.018	1.098
100			1.002	1.063	1.047	1.146
110	0.994	1.024	1.000	1.098	1.062	1.176

Following comparisons with CFD analyses and experimental data, the following modifications to the Hudson methodology are implemented into the EMBlast method:

- Clearing waves are neglected for values of $\eta > 1$.
- When the target point is located exactly at a free edge ($\eta = 0$), the reflected pressure $p_r(t)$ values drop to the free-field pressure $p_{so}(t)$ values once the clearing wave arrives. Since in this case the clearing time is practically zero, only the free-field pressure is considered in the calculation procedure.
- When two waves travelling in the opposite direction overlap, clearing is calculated only from the nearest edge.
- The free-field negative phase pressure-time history is used in the superposition with the pressure-relief clearing waves, as the reflected negative pressures result in overestimating the clearing effect.
- The pressure should not return to positive overpressures after the negative phase. For such cases, pressures are set to zero thereafter.
- Clearing from a side or top free edge is ignored if the distance from the free edge to the target point exceeds the height or width of the finite surface, respectively.
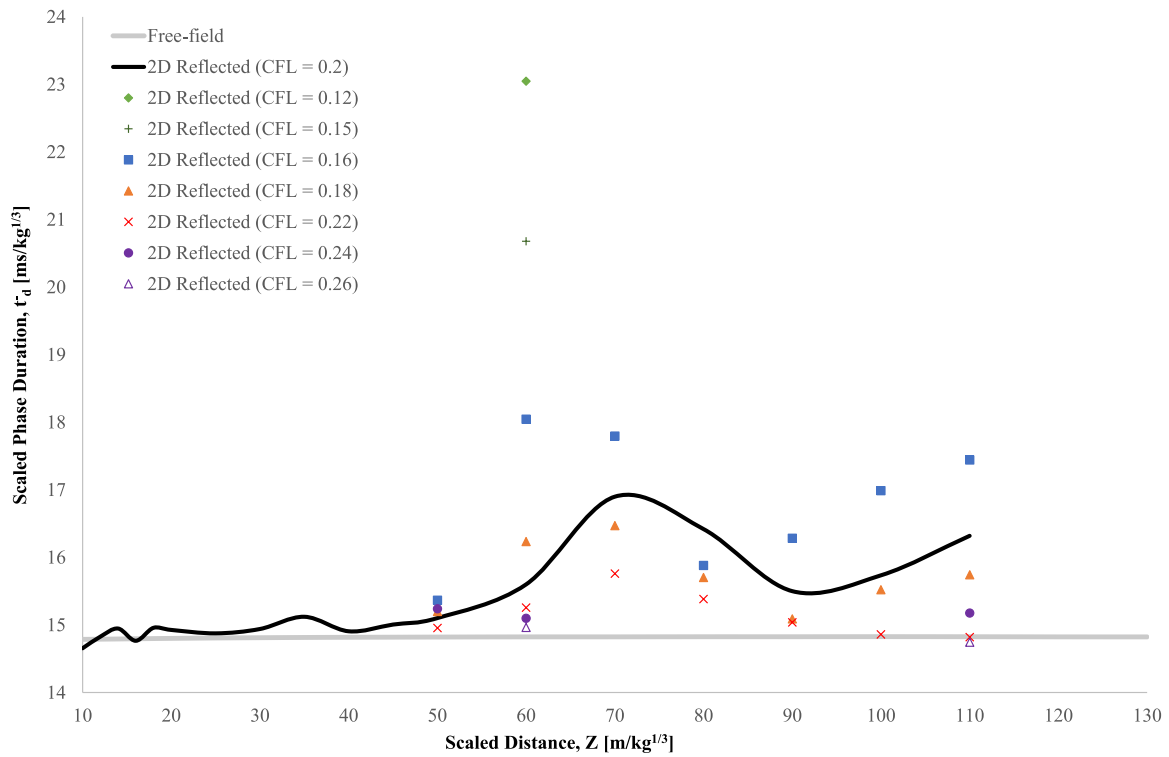
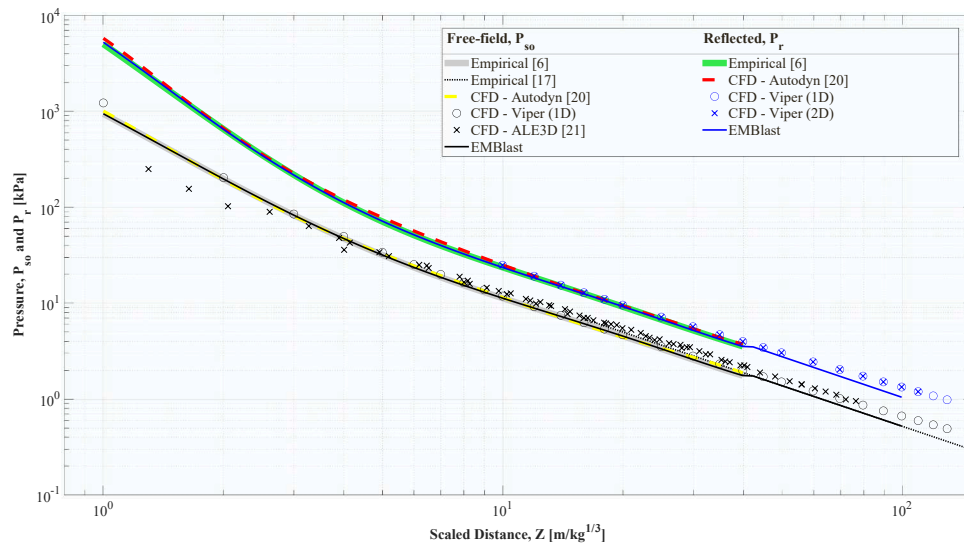**Fig. 11.** Sensitivity of the 2D reflected negative phase duration with variation of the CFL number.

Fig. 12. Comparison of EMBlast peak positive free-field P_{so} and reflected P_r pressure predictions for free-air bursts with results from empirical methods and CFD analyses.

- For a structure sitting on the ground, the ground-reflection of the clearing wave from the top edge is accounted for by placing the bottom clearing edge at a level below ground equal to the overall height of the finite surface. In this case, if the distance from the bottom edge to the target point is greater than the width of the bottom edge, then the pressure relief due to clearing from that edge is ignored.

3. Numerical validation

The CFD analysis was undertaken using the Viper::Blast CFD code. This code offers 1D, 2D and 3D modelling options with remapping capabilities between them. Both free-field and reflected analyses are performed, as described in the following sections.

3.1. Free-field blast loading

A 1 kg free-air burst was modelled with the 1D spherical expansion mode on a 150 m domain that was uniformly discretised with 1 mm cells, resulting in 150,000 cells in total. Twenty-nine gauges were placed to record the free-field pressures at the following intervals: 1 m interval from 1 m to 10 m standoff distances; 2 m interval from 10 m to 20 m standoff distances; 5 m interval from 20 m to 50 m standoff distances; and 10 m interval from 50 m to 130 m standoff distances. The analysis
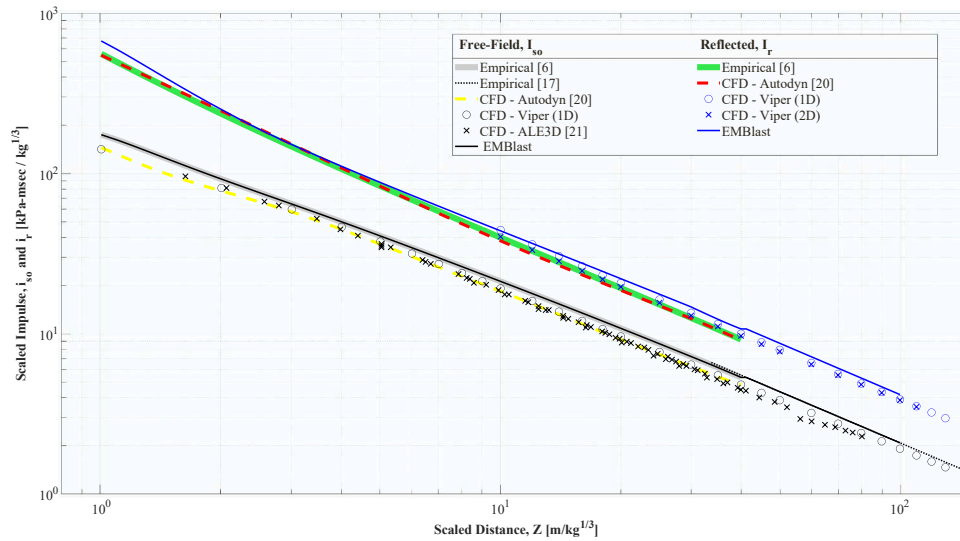
Fig. 13. Comparison of EMBlast peak positive free-field i_{so} and reflected i_r impulse predictions for free-air bursts with results from empirical methods and CFD analyses.
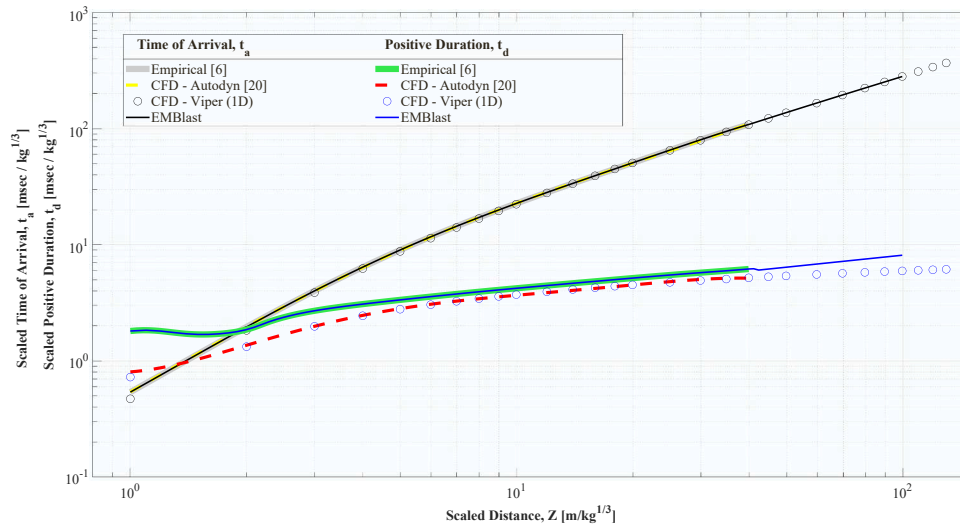

Fig. 14. Comparison of EMBlast time of arrival t_a and positive duration t_d predictions for free-air bursts with results from empirical methods and CFD analyses.

was terminated when the blast wave front reached the far edge boundary of the model, with the additional 20 m domain space modelled beyond the last gauge at the 130 m standoff distance ensuring that the complete pressure-time history (i.e. both the positive and negative phase) is recorded at all gauges prior to the analysis termination. The default Viper density of 1600 kg/m³ was prescribed for the TNT charge that results in a sphere of radius 53.04 mm. In practice, Viper slightly modifies the density to model only an integer number of cells with the TNT properties (in this case, 53). The remaining domain, corresponding to the air, was modelled as an ideal gas with ambient pressure of $P_0 = 101.325$ kPa at a temperature of 15 °C. A 0.5 value was prescribed for the Courant-Friedriches-Lewy (CFL) numerical stability control number that resulted in pressure-time histories without oscillation "noise". A simple isothermal burst model was adopted for the TNT, where the volume of the charge is converted into an ideal gas at the start of the analysis with the same density as the solid but with a detonation energy of 5.4 MJ/kg added. This value is given in the LLNL handbook [27] for the theoretical TNT heat of detonation with H_2O products as gas. This is the default Viper value for the Jones-Wilkins-Lee (JWL) equation of state, but is higher than the 4.52 MJ/kg default value for the

isothermal burst. The Viper detonation energy value was chosen as, of the various published values, it yielded the best convergence with the Kingery & Bulmash [6] empirically derived blast parameters described in Section 1. The pressure-time histories were integrated numerically to derive the impulse-time histories, and then the following blast parameters were extracted: peak positive and negative pressures and impulses, time of arrival and positive and negative phase durations.

3.2. Reflected blast loading

Two different analyses types were performed and compared for the derivation of the reflected pressure-time histories. The first was a 1D model, with the same input conditions as the free-field analyses described in Section 3.1. However, instead of the outflow boundary, a reflecting boundary surface was modelled at the end of a 1D domain, with gauges placed 0.1 mm away from the boundary. Only scaled distances $Z \geq 10$ m/kg$^{1/3}$ were considered to avoid distortions to the near-field negative phases, as a consequence of the reflected wave converging spherically rather than diverging.

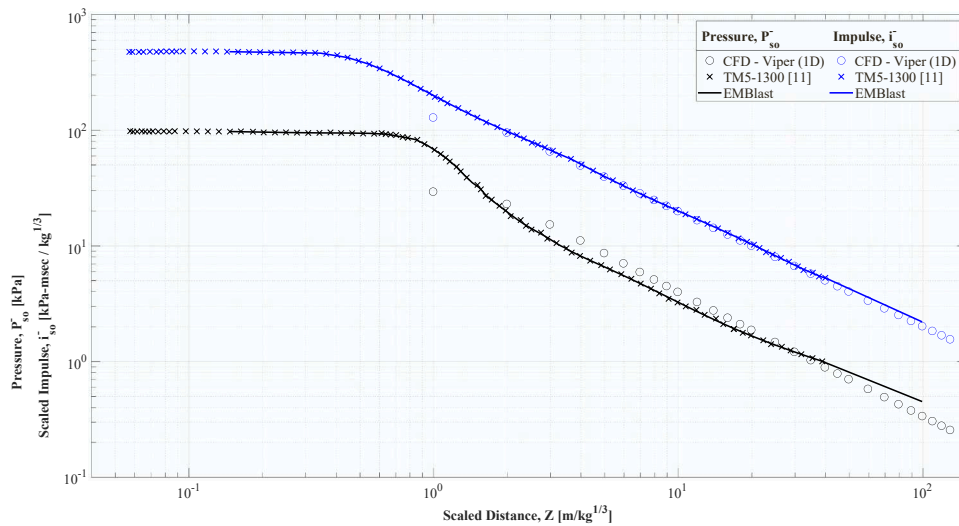In the second analysis type, a hybrid approach was considered with

Fig. 15. Comparison of EMBlast peak negative free-field pressure P_{so}^- and impulse i_{so}^- predictions for free-air bursts with results from empirical methods and CFD analyses.
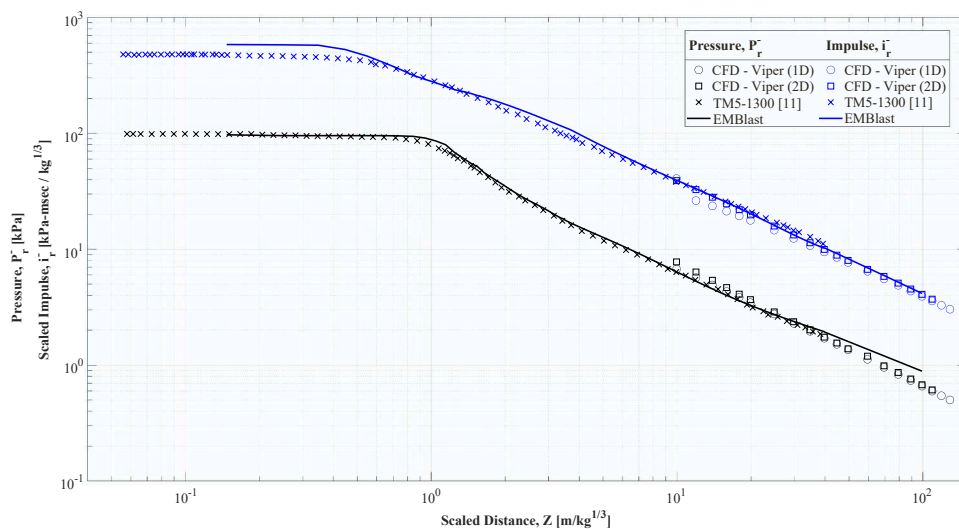

Fig. 16. Comparison of EMBlast peak negative reflected pressure P_r^- and impulse i_r^- predictions for free-air bursts with results from empirical methods and CFD analyses.

the 1D free-field analyses terminated and remapped into a 2D cylindrical model just short of reflection, when pressure change was detected 4 mm prior to the target standoff distance. In the subsequent 2D model, a flat circular reflecting boundary surface was prescribed at the domain end. The wedge domain size ranged from 8 m long by 8 m radius to 11 m long by 13 m radius, with the largest sizes corresponding to greater standoff distances. These sizes ensured that the length and radius of the model are sufficiently greater than the blast wavelength, ensuring the full negative wave has reflected, prior to any perturbation occurring from the diagonal reflection on an outflow boundary surfaces reaching the gauge. A single gauge was positioned in each 2D model 0.1 mm from the reflecting boundary. It was found that oscillation was exaggerated on the axis of symmetry, so the gauge was offset by 5 mm to reduce oscillation in the measurement without significantly affecting the range and angle of reflection. A CFL value of 0.2 was chosen through trial and error to avoid large oscillations in the negative phase pressure-time history. The choice of the CFL factor is further assessed in Section 4.1. A 2 mm mesh was applied for the 2D model, resulting in the total number of cells ranging from 16 to 36 million, depending on the standoff distance. For three scaled distances ranging from 10 m/kg$^{1/3}$ $\leq Z \leq$ 20 m/kg$^{1/3}$, the

analyses were repeated with a finer 1 mm mesh. The average differences between the 1 mm and 2 mm meshes were 0.83% for negative pressure P_r^-, 0.14% for negative impulse i_r^-, 0.08% for positive pressure P_r and 0.01% for positive impulse i_r. The normal acceptance level for adequate mesh convergence for blast loading in the coarser mesh is less than 10% difference from a finer mesh with half the cell size. Therefore, the 2 mm mesh is extremely well converged.

4. Results and discussion

This section presents the results of the CFD analyses described in Section 3. These results, along with published blast tests, existing empirical methods and CFD simulations identified in the literature, which were described in Section 1, are compared with the predictions of the EMBlast method introduced in Section 2.

4.1. CFD results

The 1D free-field pressure-time histories recorded at various scaled distance are presented Fig. 7. As sloping of the instant blast pressure rise
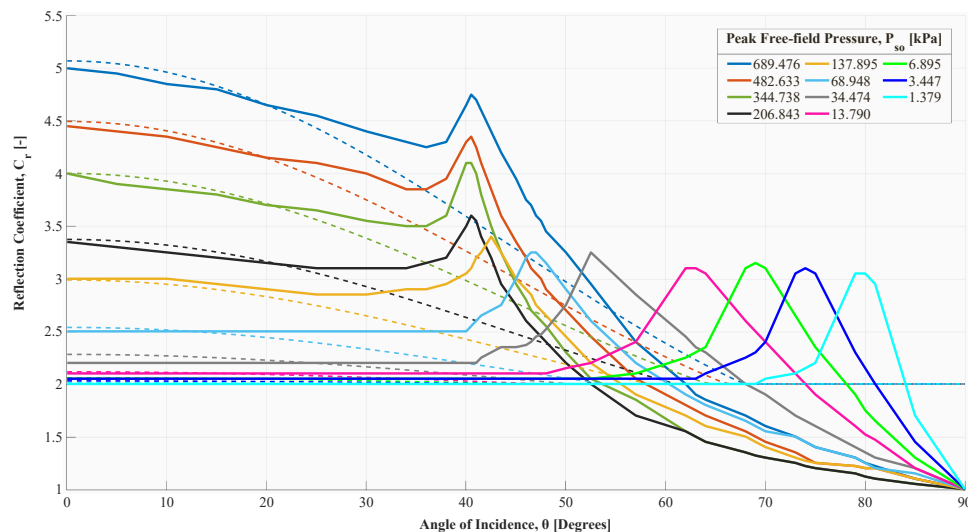
Fig. 17. Comparison of EMBlast peak pressure reflection coefficient C_r predictions for free-air bursts, as a function of angle of incidence θ and peak free-field positive pressure P_{so}, with the UFC 3–340–02 empirical method. Solid lines denote the UFC 3–340–02 empirical graphs and dashed lines the EMBlast predictions.

is observed in this figure, the time of arrival t_a is taken as the average of the time that the pressure first lifts above ambient and the time of peak incident pressure P_{so}. The average Viper positive free-field peak pressure P_{so} and impulse i_{so} values over the scale distances 1 m/kg$^{1/3}$ $\leq Z \leq 35$ m/kg$^{1/3}$ is 106.6% and 89.8%, respectively, of the Kingery & Bulmash [6] empirical values, with the CFD results consistently underpredicting the Kingery & Bulmash impulse i_{so} values. Refer to Table 1 for a tabulated comparison. This conclusion was also observed by Shin et al. [20] and Taylor [21], who performed CFD simulations with Autodyn and ALE3D, respectively, as discussed in Section 1.

The 2D reflection analyses show the limitations of the 1D reflection model, which effectively models the reflection from a concave spherical surface rather than a plane surface. As observed from Fig. 8, at lower scaled distances the 1D positive and negative reflected impulse values diverge from the linear (log-log axes) relationship of the free-field values. Furthermore, the positive and negative phase durations from the 2D reflected analyses remain very close to the free-field durations at lower scaled distances. On the other hand, an increase in the positive phase duration and a decrease in the negative phase duration is observed from the 1D reflected analyses in Fig. 9 at lower scaled distances. However, Fig. 9 also shows some irregular increases in the 2D negative phase duration values for scaled distances $Z \geq 60$ m/kg$^{1/3}$. These irregularities are attributed to the small, randomly varying, but increasing elements of noise observed in the pressure-time histories for larger scaled distances. The pressure-time history recorded at scaled distance $Z = 60$ m/kg$^{1/3}$ with a CFL of 0.2 is shown in Fig. 10, with some noise observed at the time of the negative peak pressure. The effect of varying the CFL value, and hence the timestep, on the negative phase duration was investigated by remapping the blast wave at standoff distances from $R = 50$ m to $R = 110$ m into a number of 2D models that were identical except for the CFL value. The normalised reflected negative phase durations, as a proportion of the free-field negative durations, are presented in Table 2 and Fig. 11. The results show that lower CFL, and therefore larger numbers of 2D timesteps, tend to increase the duration of the negative phase, however, without a noticeable consistent trend with standoff distance. Nevertheless, this observed variability does not influence the validation of the EMBlast method, as in the latter the impulse is the critical parameter that requires validation, from which the negative phase duration is calculated iteratively, as discussed in Section 2.1.

4.2. EMBlast validation

This section presents the validation of the EMBlast method. The positive and negative phase blast parameters on infinite surfaces are first evaluated, followed by an assessment of the results for various angles of incidence. Finally, the clearing predictions on finite size targets are examined.

4.2.1. Positive phase parameters

The EMBlast predictions of the positive peak free-field P_{so} and reflected P_r pressures, positive free-field i_{so} and reflected i_r impulses, and times of arrival t_a and positive durations t_d, from free-air bursts for scaled distances 1 m/kg$^{1/3}$ $\leq Z \leq 100$ m/kg$^{1/3}$ are presented in Fig. 12, Fig. 13 and Fig. 14, respectively. These are compared with Kingery's & Bulmash's [6] and Swisdak's [17] empirical methods, indicating perfect agreement for the free-field parameters, as the same polynomial equations have been implemented in the EMBlast method, as discussed is Section 2.1. The reflected EMBlast parameters, which are based on the LAMB addition, as discussed in Section 2.2, also show good agreement with the results from the Kingery & Bulmash empirical polynomials. However, the latter are limited to scaled distances of $Z \leq 40$ m/kg$^{1/3}$.

The far-field EMBlast reflected parameters are validated with the 1D and 2D reflected Viper analyses, with the latter offering more reliable results as discussed in Section 4.1. A good agreement is observed consistently for all reflected parameters. However, EMBlast consistently overpredicts the results from the Viper free-field analyses for the impulse i_{so} and positive duration t_d. These discrepancies are attributed to the inherent conservatism, with respect to the CFD simulations, included in the empirical Kingery & Bulmash polynomials for the free-field impulse and duration, which the EMBlast method is based on. This was previously discussed in Section 1, referring to the results from CFD analyses with Autodyn [20] and ALE3D [21]. These CFD results are also plotted in Fig. 12, Fig. 13 and Fig. 14, with the scaled distances of the ALE3D results modified, by multiplying the charge mass (W) by factor of 2, to convert the modelled hard-ground surface bursts to free-air explosions. Refer to Appendix A.2 for a tabulated comparison of Figs. 12, 13 and 14.

4.2.2. Negative phase parameters

The EMBlast predictions for scaled distances 0.147 m/kg$^{1/3}$ $\leq Z \leq 100$ m/kg$^{1/3}$ of the negative peak free-field pressures P_{so}^- and impulses i_{so}^- from free-air bursts are presented in Fig. 15. As discussed in Section 2.1, these are derived from the polynomial equations presented
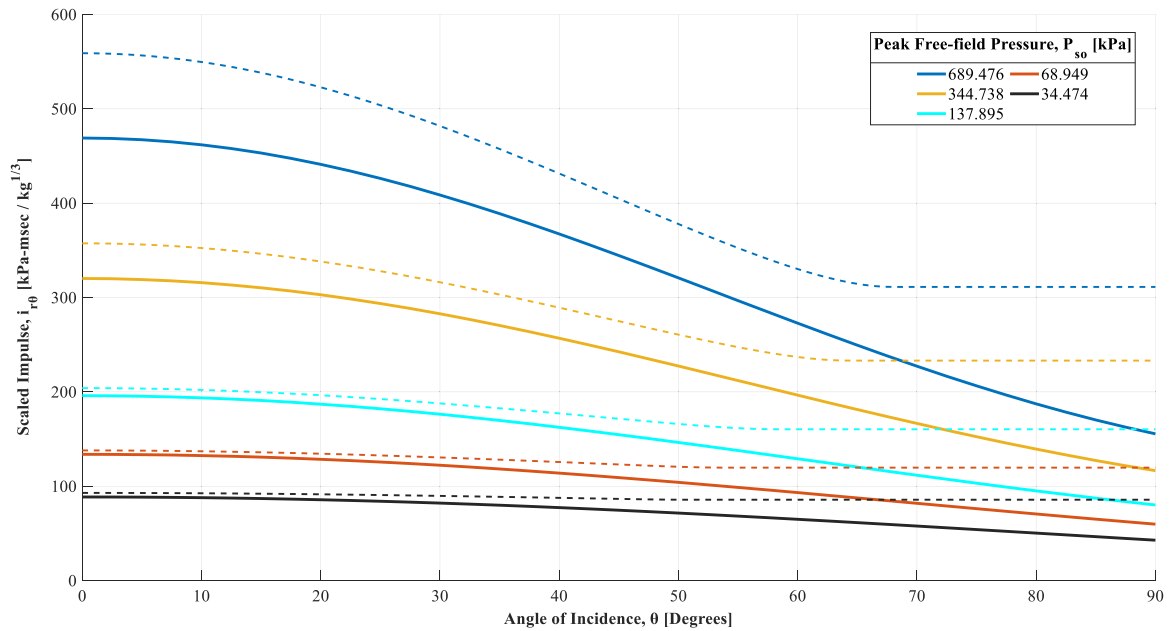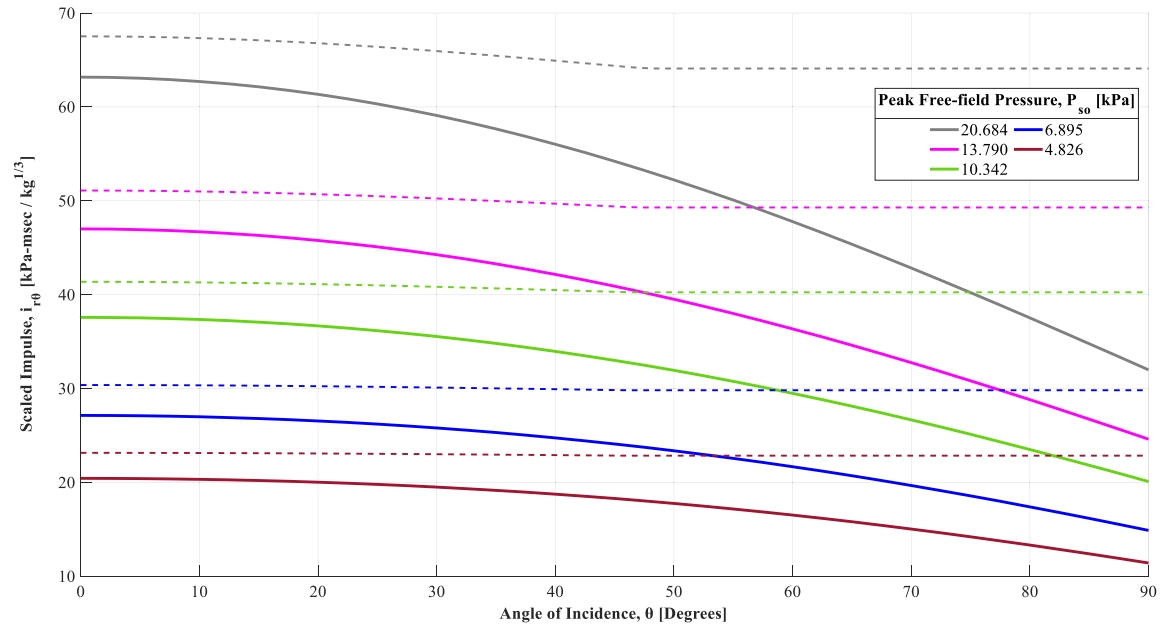
Fig. 18. Comparison of EMBlast scaled impulse $i_{r\theta}$ predictions for free-air bursts, as a function of angle of incidence θ and peak free-field positive pressure P_{so}, with the UFC 3–340–02 empirical method: a) $P_{so} \geq 34.474$ kPa (5 psi), and b) $P_{so} \leq 20.684$ kPa (3 psi). Solid lines denote the UFC 3–340–02 empirical graphs and dashed lines the EMBlast predictions.

in Appendix A.1 that have been fitted to the TM5–1300 digitised data up to scaled distance of $Z \leq 40$ m/kg$^{1/3}$ and then extrapolated to a scaled distance of $Z = 100$ m/kg$^{1/3}$. To demonstrate the accuracy of the fitted polynomial equations, the TM5–1300 digitised data are also plotted in Fig. 15. The far-field predictions beyond the TM5–1300 digitised data are validated with the results from the Viper free-field analyses. A good agreement between the EMBlast predictions and the Viper results is observed consistently in Fig. 15.

Fig. 16 presents the EMBlast predictions for the negative peak reflected pressures P_r^- and impulses i_r^- from free-air bursts for scaled distances 0.147 m/kg$^{1/3} \leq Z \leq 100$ m/kg$^{1/3}$. As discussed in Section 2.1, these are derived by applying the LAMB shock addition rules. The TM5–1300 digitised data, up to a scaled distance of $Z \leq 40$ m/kg$^{1/3}$, and

the results from the 1D and 2D Viper reflected analyses are also plotted in Fig. 16, indicating a good agreement with the EMBlast predictions consistently.

4.2.3. Angle of incidence

For targets located on a reflecting surface that is at an oblique angle to the front of the blast wave, the effect of the angle of incidence θ on the blast parameters is accounted for in the EMBlast method by Eq. 4b. The EMBlast predictions for angles of incidence ranging from $0° \leq \theta \leq 90°$ are compared in Fig. 17 and Fig. 18 with the reflection coefficient C_r and scaled impulse $i_{r\theta}$ graphs, respectively, included in UFC 3–340–02. In these figures, only the UFC 3–340–02 curves with free-field positive pressures $P_{so} \leq 689.476$ kPa (100 psi) are included that correspond to
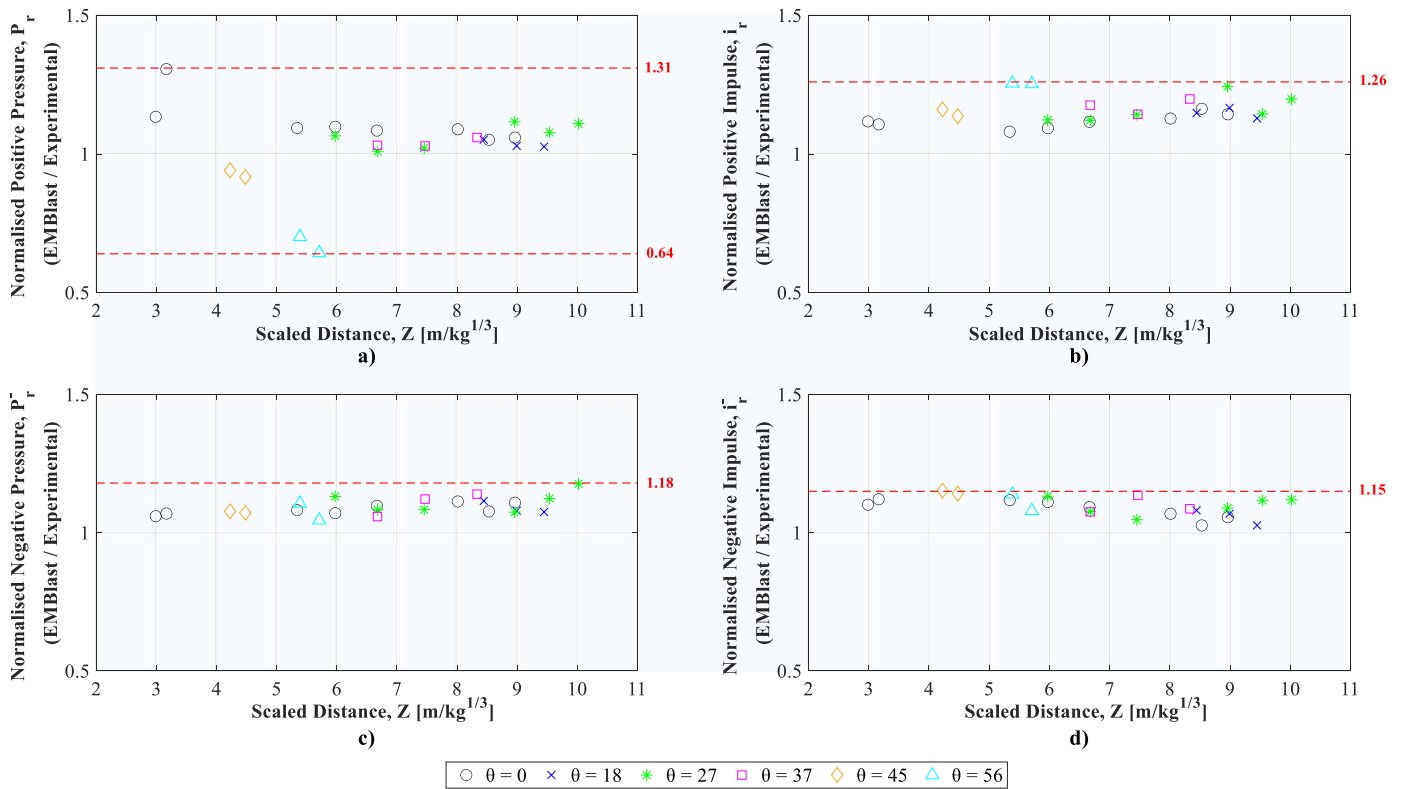
Fig. 19. Plots of normalised EMBlast predictions for surface bursts, with respect to the experimental results from Rigby et al. [12], as a function of the angle of incidence θ and scaled distance Z: a) peak positive pressure $P_{r\theta}$, b) peak positive impulse $i_{r\theta}$, c) peak negative pressure $P_{r\theta}^{-}$, and d) peak negative impulse $i_{r\theta}^{-}$.

scaled distances greater than $Z \geq 1 \; m/kg^{1/3}$. For shallow angles of incidence $\theta \leq 20°$, a good agreement between the EMBlast predictions and the UFC 3–340–02 graphs is observed in Fig. 17. However, for steeper angles ($\theta > 20°$) significant discrepancies are observed. Namely, the EMBlast method fails to replicate the formation of Mach waves, resulting from the coalescence of the incident and target-reflected wave prior to reaching the target, that are noticeable as local peaks in the UFC 3–340–02 graphs. Furthermore, for very steep angles, the reflection coefficients predicted by the EMBlast method converge to the value of $C_r = 2$, whereas the UFC 3–340–02 graphs are less conservative with recommended values as low as $C_r = 1$. Nevertheless, despite the noticeable discrepancies in the reflection coefficient predictions, the EMBlast method provides more conservative predictions of the scaled impulses $i_{r\theta}$, compared to the UFC 3–340–02 graphs, as observed in Fig. 18. This observation is consistent at all scaled distances and angles of incidence considered. This implies that the EMBlast method will result in conservative predictions for structures in the impulsive regime (typically for short duration pulses with respect to the natural period). On the other hand, further research is required to assess the accuracy of the EMBlast predictions at steep angles ($\theta > 20°$) for structures in the quasi-static regime (typically for long duration pulses with respect to the natural period), as their response is dominated by the peak reflected pressure.

The EMBlast predictions are also compared with Rigby's et al. [12] experimental work that was described in Section 1. In this comparison, a TNT equivalence factor of 1.2 was adopted to convert the PE4 charges considered in the blast trials into equivalent TNT charges. This value has shown good agreement with previous experimental results [12,24]. Furthermore, hard ground surface bursts were assumed to represent the concrete slab of the experimental conditions. Fig. 19 presents the

normalised EMBlast predictions, with respect to the averaged experimental results repeated at the same scaled distances and angle of incidences, for the peak positive pressure $P_{r\theta}$, peak positive impulse $i_{r\theta}$, peak negative pressure $P_{r\theta}^{-}$ and peak negative impulse $i_{r\theta}^{-}$. With the exception of the peak positive pressure $P_{r\theta}$ predictions at angles of incidence of $\theta = 45°$ and $56°$, a good agreement is observed consistently for all parameters at the scaled distances and angles of incidences considered, with the EMBlast results slightly overpredicting the experimental values, with normalised ratios up to 1.31, and in most cases the ratios are even closer to unity. The underpredicted EMBlast peak positive pressures $P_{r\theta}$ at angles of incidence of $\theta = 45°$ and $56°$ are most likely attributed to the failure of the EMBlast method to capture the formation of Mach waves, as previously discussed for Fig. 17. Nevertheless, the EMBlast predictions for the remaining blast parameters at the same angles of incidence show good agreement with the experimental results, as shown in Fig. 19b, c and d.

4.2.4. Clearing effects on finite target surfaces

EMBlast's clearing effect predictions on finite target surfaces are assessed in Fig. 20 and Fig. 21, by comparing the predicted pressure-time histories with the experimental results from Tyas, et al. [24] that were described in Section 1. As discussed in Section 4.2.3, a TNT equivalence factor of 1.2 was adopted to convert the PE4 charges into equivalent TNT charges, and hard ground surface bursts were assumed to represent the experimental conditions. The figures show the experimental results as averaged values over the last twenty recorded data, a practice commonly considered to smoothen the experimental pressure-time history trace. Fig. 20 presents the comparisons for a gauge placed in the middle of the concrete target surface, with the nearest free
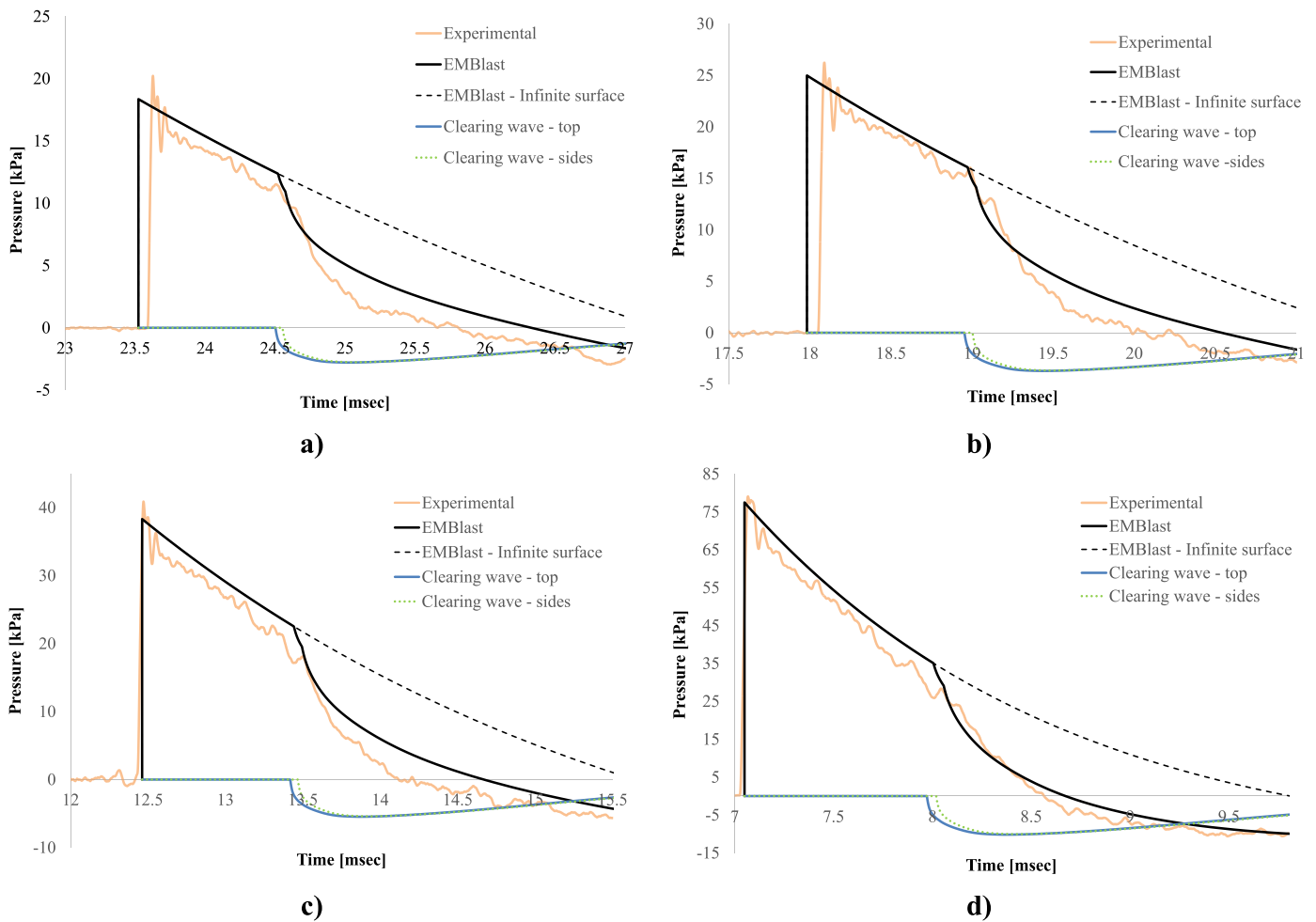
Fig. 20. Comparison of EMBlast clearing predictions with experimental results [24] for a target point located L_v = 337.5 mm and L_h = 355 mm from the top and side free edges, respectively, for various scaled distances: a) Z = 15 m/kg$^{1/3}$, b) Z = 12 m/kg$^{1/3}$, c) Z = 9 m/kg$^{1/3}$ and d) Z = 6 m/kg$^{1/3}$.

edges located L_v = 337.5 mm and L_h = 355 mm from the top and side edges. The Hudson pressure-relief waves travelling from the free edges are also shown in the figure. These are superimposed on the reflected pressure-time history, derived for an infinite surface and shown as a dashed line in the figure. A good agreement between the EMBlast predictions and the experimental results is observed in Fig. 20 for all four scaled distances considered. In Fig. 21, the comparison is made for a gauge moved closer to the top free edge, reducing the distance to L_v = 168.75 mm, while keeping the same distance to the side edges L_h = 355 mm. This results in the pressure-relief waves travelling from the top free edge arriving faster at the target point, as shown in Fig. 21. Again, the overall shape of the experimental pulse is well captured by the EMBlast method for all four scaled distances considered.

5. Conclusions

This paper has presented a fast-running method for predicting blast loads from free-air and surface burst explosions on structures in the far-field up to a scaled distance of 100 m/kg$^{1/3}$. In this method, the free-field pressure-time histories were described by the modified Friedlander and the cubic expression for the positive and negative phase, respectively. The blast parameters required by these expressions are the

peak pressure, impulse, phase duration and blast wave time of arrival. These were derived empirically as a function of scaled distance from a combination of existing empirical polynomials equations and graphs fitted to blast trial results, which are included in military standards, and suggested modifications to extend these to the far-field. The reflected pressure-time histories on infinite target surfaces were subsequently derived by applying a modified version of the semi-empirical Low Altitude Multiple Burst shock addition rules to superimpose non-linearly the free-field waves with target-reflected waves. The latter were assumed to originate from fictitious charges (image) located symmetrically to the actual charge (real), with respect to the target surface. Finally, to account for clearing effects on finite size targets, the Hudson methodology was adopted, and the reflected pressure-time histories were superimposed with pressure relief waveforms travelling from the free edges.

The predicted free-field and reflected blast parameters over a range of scaled distances from 1 m/kg$^{1/3}$ to 100 m/kg$^{1/3}$ were compared with the results from existing empirical methods and computational fluid dynamic simulations identified in the literature. These were complemented with additional free-field and reflected computational fluid dynamic analyses performed to obtain further validation data. The predicted parameters demonstrated a good agreement with the
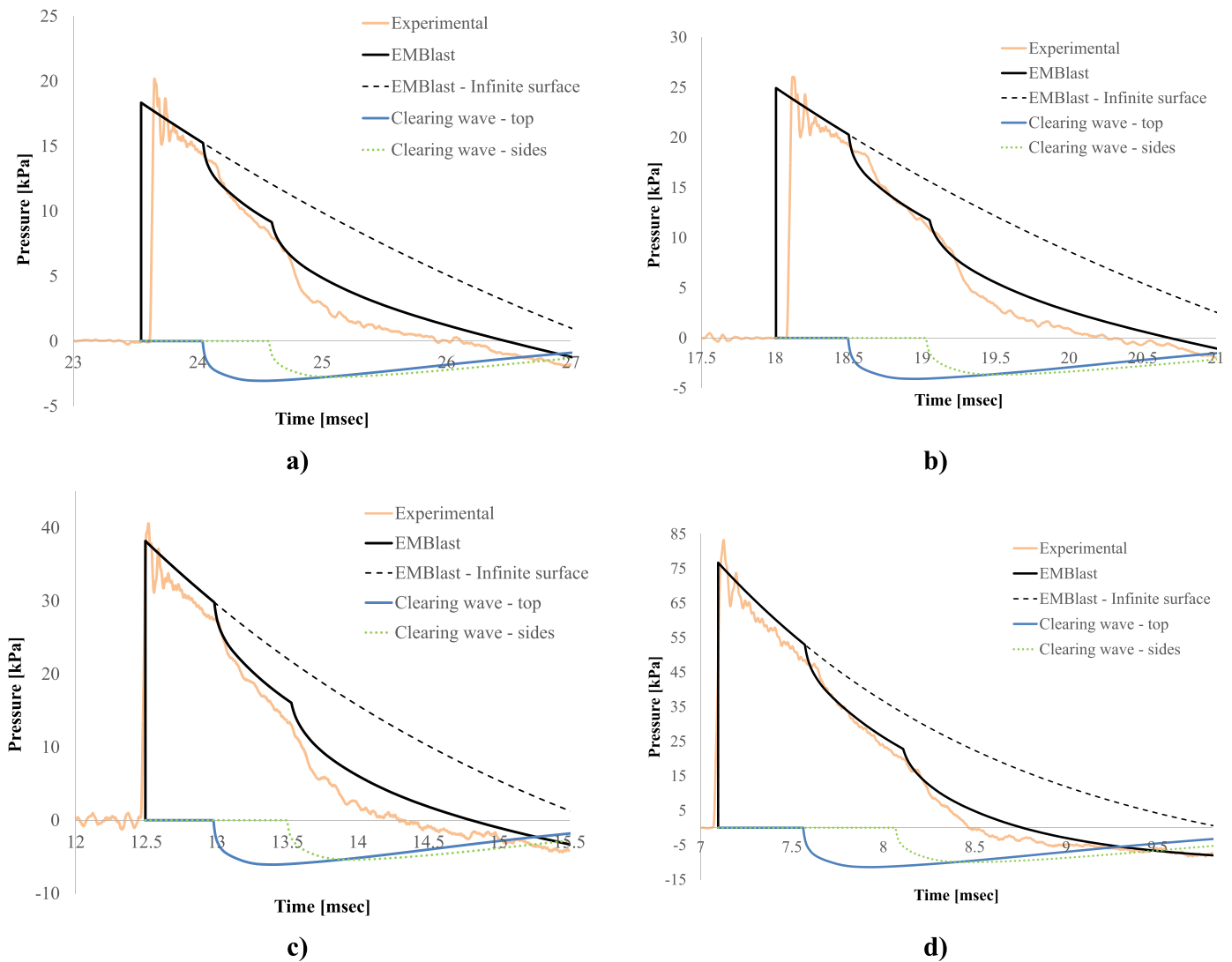
Fig. 21. Comparison of EMBlast clearing predictions with experimental results [24] for a target point located L_v = 168.75 mm and L_h = 355 mm from the top and side free edges, respectively, for various scaled distances: a) Z = 15 m/kg$^{1/3}$, b) Z = 12 m/kg$^{1/3}$, c) Z = 9 m/kg$^{1/3}$ and d) Z = 6 m/kg$^{1/3}$.

empirical methods, but consistently overpredicted the positive free-field impulses derived from the computational fluid dynamic analyses. This conclusion is consistent with the findings reported by previous researchers and is attributed to an inherent conservatism built-in in existing empirical methods. A comparison with published blast tests identified in the literature, demonstrated that the Low Altitude Multiple Burst shock addition rules and the Hudson method can offer safe and accurate predictions of the reflected pressure-time histories on target surfaces at various angles of incidence and can account for clearing effects in the far-field, respectively.

Future work will focus on extending the blast loading predictions to near-field scaled distances. This will include expanding the clearing predictions on target surfaces in the near-field, where the blast wave front is less likely to be planar and semi-analytical methods, such as the Hudson method, are less likely to yield accurate predictions.

Furthermore, above-ground explosions will also be considered, where the charge is located at a vertical distance from the ground, resulting in a complex interaction between the incident and ground-reflected waves.

Declaration of Competing Interest

The authors declare that they have no known competing financial interests or personal relationships that could have appeared to influence the work reported in this paper.

Acknowledgements

Appendix A.1. : Negative phase free-field polynomial equations

A.1.1 Free-air bursts

A.1.1.1 Peak negative pressure in kPa

- For $0.147 \frac{m}{kg^{1/3}} \leq Z < 0.71 \frac{m}{kg^{1/3}}$:

$$P_{so}^{-} = 10^{\wedge}(-0.2730366858(\log_{10}Z)^6 - 1.8528194712(\log_{10}Z)^5 - 4.4891130939(\log_{10}Z)^4$$

$$-5.1136435596(\log_{10}Z)^3 - 2.914453356(\log_{10}Z)^2 - 0.8139165864\log_{10}Z + 1.8922432283)$$

- For $0.71 \frac{m}{kg^{1/3}} \leq Z < 1.52 \frac{m}{kg^{1/3}}$:

$$P_{so}^{-} = 10^{\wedge}(7309.5396845341(\log_{10}Z)^6 - 372.0356631663(\log_{10}Z)^5 - 240.9205874618(\log_{10}Z)^4$$

$$-11.9080637575(\log_{10}Z)^3 - 1.719829479(\log_{10}Z)^2 - 1.3914840214\log_{10}Z + 1.8427257303)$$

- For $1.52 \quad \frac{m}{kg^{1/3}} \leq Z < 3.52 \frac{m}{kg^{1/3}}$:

$$P_{so}^{-} = 10^{\wedge}(3449.8858503103(\log_{10}Z)^6 - 7658.7863767242(\log_{10}Z)^5 + 6933.7487977224(\log_{10}Z)^4$$

$$-3274.5782062742(\log_{10}Z)^3 + 851.7249448683(\log_{10}Z)^2 - 117.4868281157\log_{10}Z + 8.2379977943)$$

- For $3.52 \frac{m}{kg^{1/3}} \leq Z \leq 40 \frac{m}{kg^{1/3}}$:

$$P_{so}^{-} = 10^{\wedge}(1.4846015234(\log_{10}Z)^6 - 10.6897731555(\log_{10}Z)^5 + 31.028077977(\log_{10}Z)^4$$

$$-46.103092737(\log_{10}Z)^3 + 36.8435251144(\log_{10}Z)^2 - 16.0018409958\log_{10}Z + 3.9537261061)$$

- $40 \frac{m}{kg^{1/3}} < Z < 100 \frac{m}{kg^{1/3}}$:

$$P_{so}^{-} = 10^{\wedge}(-0.85427\log_{10}Z + 1.359581)$$

A.1.1.2 Scaled peak negative impulse in kPa-msec / $kg^{1/3}$

- For $0.147 \frac{m}{kg^{1/3}} \leq Z < 0.329 \frac{m}{kg^{1/3}}$:

$$\frac{i_{so}^{-}}{W^{1/3}} = 10^{\wedge}(-2.1495511029(\log_{10}Z)^6 - 12.6467583464(\log_{10}Z)^5 - 29.8080137616(\log_{10}Z)^4$$

$$-35.9505116276(\log_{10}Z)^3 - 23.3852447966(\log_{10}Z)^2 - 7.8063047587\log_{10}Z + 1.6291406098)$$

- For $0.329 \frac{m}{kg^{1/3}} \leq Z < 3.663 \frac{m}{kg^{1/3}}$:

$$\frac{i_{so}^{-}}{W^{1/3}} = 10^{\wedge}(3.4374291992(\log_{10}Z)^6 - 1.5446189879(\log_{10}Z)^5 - 2.2899793179(\log_{10}Z)^4$$

$$+1.4383160113(\log_{10}Z)^3 + 0.11191091612(\log_{10}Z)^2 - 1.1302973197\log_{10}Z + 2.3085344835)$$

- For $3.663 \frac{m}{kg^{1/3}} \leq Z \leq 40 \frac{m}{kg^{1/3}}$:

$$\frac{i_{so}^{-}}{W^{1/3}} = 10^{\wedge}(0.8639854323(\log_{10}Z)^6 - 4.5256932938(\log_{10}Z)^5 + 9.4231025149(\log_{10}Z)^4$$

$$-10.1971903801(\log_{10}Z)^3 + 6.420101876(\log_{10}Z)^2 - 3.4354497051\log_{10}Z + 2.7586702448)$$

- $40 \frac{m}{kg^{1/3}} < Z < 100 \frac{m}{kg^{1/3}}$:

$$\frac{i_{so}^-}{W^{1/3}} = 10^\wedge(-0.96415\log_{10}Z + 2.270918)$$

A.1.2 Soft-ground surface bursts

A.1.2.1 Peak negative pressure in kPa

- For $0.178\frac{\mathrm{m}}{\mathrm{kg}^{1/3}} \le Z < 0.65\frac{\mathrm{m}}{\mathrm{kg}^{1/3}}$:

$$P_{so}^- = 10^\wedge(-2.7579019484(\log_{10}Z)^6 - 10.4470045806(\log_{10}Z)^5 - 15.5496572668(\log_{10}Z)^4$$

$$-11.5389499511(\log_{10}Z)^3 - 4.4665073781(\log_{10}Z)^2 - 0.8591115363\log_{10}Z + 1.9467923983)$$

- For $0.65\frac{\mathrm{m}}{\mathrm{kg}^{1/3}} \le Z < 1.114\frac{\mathrm{m}}{\mathrm{kg}^{1/3}}$:

$$P_{so}^- = 10^\wedge(4998.8033981323(\log_{10}Z)^6 + 2841.8093371257(\log_{10}Z)^5 + 609.2730447144(\log_{10}Z)^4$$

$$+46.2078025394(\log_{10}Z)^3 - 4.6958953566(\log_{10}Z)^2 - 1.3641762671\log_{10}Z + 1.912027161)$$

- For $1.114 \quad \frac{\mathrm{m}}{\mathrm{kg}^{1/3}} \le Z < 3.18\frac{\mathrm{m}}{\mathrm{kg}^{1/3}}$:

$$P_{so}^- = 10^\wedge(655.8038883507(\log_{10}Z)^6 - 1110.1036023357(\log_{10}Z)^5 + 713.7227359711(\log_{10}Z)^4$$

$$-212.4217213747(\log_{10}Z)^3 + 29.1358907466(\log_{10}Z)^2 - 3.4956237069\log_{10}Z + 1.9607462388)$$

- For $3.18\frac{\mathrm{m}}{\mathrm{kg}^{1/3}} \le Z \le 40\frac{\mathrm{m}}{\mathrm{kg}^{1/3}}$:

$$P_{so}^- = 10^\wedge(-0.4548198452(\log_{10}Z)^6 + 3.3298441852(\log_{10}Z)^5 - 9.992760923(\log_{10}Z)^4$$

$$+15.6629917096(\log_{10}Z)^3 - 13.2837405397(\log_{10}Z)^2 + 4.676628528\log_{10}Z + 0.6596773452)$$

- $40\frac{\mathrm{m}}{\mathrm{kg}^{1/3}} < Z < 100\frac{\mathrm{m}}{\mathrm{kg}^{1/3}}$:

$$P_{so}^- = 10^\wedge(-0.81906\log_{10}Z + 1.40005)$$

A.1.2.2 Scaled peak negative impulse in kPa-msec / kg^{1/3}

- For $0.178\frac{\mathrm{m}}{\mathrm{kg}^{1/3}} \le Z < 0.381\frac{\mathrm{m}}{\mathrm{kg}^{1/3}}$:

$$\frac{i_{so}^-}{W^{1/3}} = 10^\wedge(6.0417439155(\log_{10}Z)^6 + 29.5712122847(\log_{10}Z)^5 + 58.7574316364(\log_{10}Z)^4$$

$$+60.5122614402(\log_{10}Z)^3 + 33.9590995506(\log_{10}Z)^2 + 9.798735201\log_{10}Z + 3.9191002762)$$

- For $0.381\frac{\mathrm{m}}{\mathrm{kg}^{1/3}} \le Z < 0.83\frac{\mathrm{m}}{\mathrm{kg}^{1/3}}$:

$$\frac{i_{so}^-}{W^{1/3}} = 10^\wedge(2165.0947294235(\log_{10}Z)^6 + 3413.654610595(\log_{10}Z)^5 + 2147.1033524135(\log_{10}Z)^4$$

$$+683.5011063802(\log_{10}Z)^3 + 113.5673124861(\log_{10}Z)^2 + 8.3673578239\log_{10}Z + 2.8233300143)$$

- For $0.83\frac{\mathrm{m}}{\mathrm{kg}^{1/3}} \le Z < 14.72\frac{\mathrm{m}}{\mathrm{kg}^{1/3}}$:

$$\frac{i_{so}^-}{W^{1/3}} = 10^\wedge(-1.7314429274(\log_{10}Z)^6 + 7.1620267303(\log_{10}Z)^5 - 10.492366666(\log_{10}Z)^4$$

$$+6.3645041193(\log_{10}Z)^3 - 1.2701215009(\log_{10}Z)^2 - 1.079345942\log_{10}Z + 2.5310170868)$$

- For $14.72 \frac{m}{kg^{1/3}} \leq Z \leq 40 \frac{m}{kg^{1/3}}$:

$$\frac{i_{so}^-}{W^{1/3}} = 10^{\wedge}(298.0288612247(\log_{10}Z)^6 - 2483.517730978(\log_{10}Z)^5 + 8614.4636096708(\log_{10}Z)^4$$

$$- 15919.8011062479(\log_{10}Z)^3 + 16531.2389338481(\log_{10}Z)^2 - 9146.0432935621\log_{10}Z + 2107.8985090143)$$

- $40 \frac{m}{kg^{1/3}} < Z < 100 \frac{m}{kg^{1/3}}$:

$$\frac{i_{so}^-}{W^{1/3}} = 10^{\wedge}(-0.85329\log_{10}Z + 2.32416)$$

Appendix A.2. : Tabulated comparison of EMBlast predictions

Table A.1

Comparison of EMBlast peak positive free-field P_{so} pressure predictions for free-air bursts with results from empirical methods and CFD analyses.

SCALED DISTANCE, Z [m/kg$^{1/3}$]	PEAK PRESSURE, P_{so} [kPa]				
	EMBlast	Empirical		CFD	
		Kingery & Bulmash[6]	Swisdak[17]	Viper (1D)	Autodyn [20]
1	934.861	934.861		1214.041	998.509
5	31.296	31.296		33.346	32.105
10	11.091	11.091		11.648	11.265
20	4.451	4.451	4.909	4.593	4.349
30	2.533	2.533	2.775	2.752	2.673
40	1.720	1.720	1.852	1.932	1.837
50	1.353		1.353	1.477	
60	1.047		1.047	1.188	
70	0.843		0.843	0.989	
80	0.698		0.698	0.845	
90	0.592		0.592	0.736	
100	0.510		0.510	0.651	

Table A.2

Comparison of EMBlast peak positive reflected P_r pressure predictions for free-air bursts with results from empirical methods and CFD analyses.

SCALED DISTANCE, Z [m/kg$^{1/3}$]	PEAK PRESSURE, P_r [kPa]				
	EMBlast	Empirical	CFD		
		Kingery & Bulmash[6]	Viper (1D)	Viper (2D)	Autodyn [20]
1	5221.465	5005.579			5746.251
5	70.623	70.022			77.001
10	23.219	23.313	24.476	24.471	24.658
20	9.071	9.033	9.376	9.377	9.210
30	5.122	5.119	5.574	5.573	5.325
40	3.466	3.479	3.899	3.899	3.688
50	2.721		2.976	2.975	
60	2.103		2.390	2.389	
70	1.692		1.988	1.988	
80	1.401		1.698	1.697	
90	1.187		1.477	1.477	
100	1.023		1.306	1.306	

Table A.3

Comparison of EMBlast peak positive free-field i_{so} impulse predictions for free-air bursts with results from empirical methods and CFD analyses.

SCALED DISTANCE, Z [m/kg$^{1/3}$]	PEAK IMPULSE, i_{so} [kPa-msec]				
	EMBlast	Empirical		CFD	
		Kingery & Bulmash[6]	Swisdak[17]	Viper	Autodyn[20]
1	174.543	174.543		141.583	144.987
5	40.619	40.619		37.586	36.079
10	21.131	21.131		19.100	18.326
20	10.752	10.752		9.568	9.157
30	7.162	7.162		6.376	6.204
40	5.304	5.304	5.475	4.779	4.783
50	4.320		4.320	3.821	
60	3.559		3.559	3.181	

Table A.3 (*continued*)

SCALED DISTANCE, Z [m/kg$^{1/3}$]	PEAK IMPULSE, i_{so} [kPa-msec]				
	EMBlast	Empirical		CFD	
		Kingery & Bulmash[6]	Swisdak[17]	Viper	Autodyn[20]
70	3.022		3.022	2.724	
80	2.622		2.622	2.381	
90	2.314		2.314	2.114	
100	2.069		2.069	1.900	

Table A.4

Comparison of EMBlast peak positive reflected i_r impulse predictions for free-air bursts with results from empirical methods and CFD analyses.

SCALED DISTANCE, Z [m/kg$^{1/3}$]	PEAK IMPULSE, i_r [kPa-msec]				
	EMBlast	Empirical	CFD		
		Kingery & Bulmash[6]	Viper (1D)	Viper (2D)	Autodyn[20]
1	672.854	559.034			547.716
5	87.751	83.317			83.028
10	43.732	39.715	44.234	40.216	37.884
20	21.971	19.179	20.642	19.542	18.585
30	14.623	12.485	13.431	12.917	12.369
40	10.657	9.162	9.945	9.646	9.058
50	8.673		7.892	7.697	
60	7.140		6.538	6.402	
70	6.058		5.578	5.478	
80	5.255		4.862	4.786	
90	4.636		4.307	4.249	
100	4.144		3.865	3.820	

Table A.5

Comparison of EMBlast time of arrival t_a predictions for free-air bursts with results from empirical methods and CFD analyses.

SCALED DISTANCE, Z [m/kg$^{1/3}$]	TIME OF ARRIVAL, t_a [msec]			
	EMBlast	Empirical	CFD	
		Kingery & Bulmash[6]	Viper (1D)	Autodyn [20]
1	0.532	0.532	0.466	0.534
5	8.995	8.995	8.753	8.936
10	22.722	22.722	22.382	22.810
20	50.968	50.968	50.921	50.678
30	80.620	80.620	79.884	79.342
40	109.486	109.486	108.996	110.620
50	138.641		138.183	
60	167.795		167.416	
70	196.950		196.679	
80	226.104		225.965	
90	255.259		255.266	
100	284.413		284.580	

Table A.6

Comparison of EMBlast positive phase duration t_d predictions for free-air bursts with results from empirical methods and CFD analyses.

SCALED DISTANCE, Z [m/kg$^{1/3}$]	POSITIVE PHASE DURATION, t_d [msec]			
	EMBlast	Empirical	CFD	
		Kingery & Bulmash[6]	Viper (1D)	Autodyn [20]
1	1.795	1.795	0.717	0.795
5	3.333	3.333	2.769	2.799
10	4.200	4.200	3.705	3.655
20	5.142	5.142	4.495	4.485
30	5.731	5.731	4.904	5.011
40	6.165	6.165	5.174	5.133
50	6.387		5.375	
60	6.801		5.531	
70	7.172		5.660	
80	7.510		5.766	
90	7.821		5.857	
100	8.110		5.935	

References

[1] Rigby SE, Lodge TJ, Alotaibi S, Barr AD, Clarke SD, Langdon GS, et al. Preliminary yield estimation of the 2020 Beirut explosion using video footage from social media. Shock Waves 2020;30:671–5. https://doi.org/10.1007/s00193-020-00970-z.

[2] Angelides, S.C., Talbot, J.P.: Blast response of laminated glass panels: a critical review of analysis and design methods. Proceedings of the Institution of Civil Engineers – Structures and Buildings (2022). https://doi.org/10.1680/jstbu.20.00248.

[3] Burgan, B.A., Pilpilidou, A.: SCI P415 Design of Low To Medium Rise Buildings Against External Explosions, Ascot: SCI (2018).

[4] Rigby SE, Tyas A, Clarke SD, Fay SD, Reay JJ, Warren JA, et al. The negative phase of the blast load. Int J Prot Struct 2014;5(1):1–19. https://doi.org/10.1260/2041-4196.5.1.1.

[5] Rigby SE, Tyas A, Bennett T, Fay SD, Clarke SD, Warren JA. A numerical investigation of blast loading and clearing on small targets. Int J Prot Struct 2014;5(3). https://doi.org/10.1260/2041-4196.5.3.253.

[6] Kingery, C.N., Bulmash, G.: ARBRL-TR-02555 Airblast Parameters from TNT Spherical Air Burst and Hemispherical Surface Burst (1984).

[7] UFC 3–340-01: Design and Analysis of Hardened Structures to Conventional Weapons Effects. US Army Corps of Engineers (2002).

[8] UFC 3–340-02: Structures to Resist the Effects of Accidental Explosives. US Army Corps of Engineers (2014).

[9] Hyde, D.W.: Conventional Weapons Program (ConWep), U.S Army Waterways Experimental Station, Vicksburg, (1991).

[10] Rigby, S.E. , Tyas, A. , Clarke, S.D. , Fay, S.D. , Reay, J.J. , Warren, J.A. , et al. A Review of UFC-3-340-02 Blast Wave Clearing Predictions. In: Proceedings of 16th International Symposium for the Interaction of the Effects of Munitions with Structures, Destin (2015).

[11] TM5-1300: Structures to Resist the Effects of Accidental Explosions. US Army Corps of Engineers (1990).

[12] Rigby SE, Fay SD, Tyas A, Warren JA, Clarke SD. Angle of incidence effects on far-field positive and negative phase blast parameters. Int J Prot Struct 2015;6(1):23–42. https://doi.org/10.1260/2041-4196.6.1.23.

[13] ISO 16933:2007: Glass in building — Explosion-resistant security glazing — Test and classification for arena air-blast loading, ISO (2007).

[14] ASCE/SEI 59–22: Blast protection of buildings, ASCE (2023).

[15] Locking, P.M.: The trouble with TNT equivalence. In: Proceedings of 26th International Symposium on Ballistics, Miami (2011).

[16] Locking, P.M.: TNT equivalence—experimental comparison against prediction. In: Proceedings of 27th International Symposium on Ballistics, Freiburg (2013).

[17] Swisdak Jr., M.M.: Simplified Kingery Airblast Calculations (1994).

[18] Kingery, C.N., Pannill, B.F.: AD443102 Peak Overpressure Vs Scaled Distance for TNT Surface Bursts (Hemispherical Charges) (1964).

[19] Valsamos G, Larcher M, Casadei F. Beirut explosion 2020: a case study for a large-scale urban blast simulation. Saf Sci 2021;137. https://doi.org/10.1016/j.ssci.2021.105190.

[20] Shin J, Whittaker AS, Cormie D. Incident and normally reflected overpressure and impulse for detonations of spherical high explosives in free Air. J Struct Eng 2015;141(12).

[21] Taylor AG. Numerical analysis of blast effects and mitigation in the far-field from small explosions. Appl Sci 2022;12:8824. https://doi.org/10.3390/app12178824.

[22] Hikida, S., Needham, C.E.: Low Altitude Multiple Burst (LAMB) Model: Volume I - Shock Description (1981).

[23] Hudson, C.C.: SC-TM-191–55-51: Sound pulse approximations to blast loading (with comments on transient drag). Sandia Corporation Technical Memorandum (1955). https://www.osti.gov/opennet/servlets/purl/16340913-1cPgoX/16340913.pdf.

[24] Tyas A, Warren JA, Bennett T, Fay S. Prediction of clearing effects in far-field blast loading of finite targets. Shock Waves 2011;21:111–9. https://doi.org/10.1007/s00193-011-0308-0.

[25] Rigby, S.E.: Blast Wave Clearing Effects on Finite-Sized Targets Subjected to Explosive Loads. Ph.D. Dissertation. University of Sheffield, Sheffield (2014).

[26] Nartu MK, Kumar M, Ramisetti SB. Improved methodology for accurate prediction of blast wave clearing on a finite target. J Eng Mech 2022;148(9). https://doi.org/10.1061/(ASCE)EM.1943-7889.0002134.

[27] Dobratz, B.M.: LLNL Explosives Handbook. Lawrence Livermore National Laboratory (1981).